Title
A spatially resolved surface kinetic model for forsterite dissolution

Authors
Maher, Kate
Johnson, Natalie C
Jackson, Ariel
et al.

Publication Date
2016-02-01

DOI
10.1016/j.gca.2015.11.019

Peer reviewed

Available online at www.sciencedirect.com

ScienceDirect

Geochimica et Cosmochimica Acta 174 (2016) 313–334

Geochimica et Cosmochimica Acta

www.elsevier.com/locate/gca

A spatially resolved surface kinetic model for forsterite dissolution

Kate Maher [a,*], Natalie C. Johnson [b], Ariel Jackson [c], Laura N. Lammers [a,1], Abe B. Torchinsky [a], Karrie L. Weaver [a], Dennis K. Bird [a], Gordon E. Brown Jr. [a,b,d]

[a] Department of Geological Sciences, Stanford University, Stanford, CA 94305-2115, USA
[b] Department of Chemical Engineering, Stanford University, Stanford, CA 94305, USA
[c] Department of Materials Science and Engineering, Stanford University, Stanford, CA 94305, USA
[d] Department of Photon Science and Stanford Synchrotron Radiation Lightsource, SLAC National Accelerator Laboratory, 2575 Sand Hill Rd., MS 69, Menlo Park, CA 94025, USA

Received 8 July 2014; accepted in revised form 4 November 2015; Available online 27 November 2015

Abstract

The development of complex alteration layers on silicate mineral surfaces undergoing dissolution is a widely observed phenomenon. Given the complexity of these layers, most kinetic models used to predict rates of mineral–fluid interactions do not explicitly consider their formation. As a result, the relationship between the development of the altered layers and the final dissolution rate is poorly understood. To improve our understanding of the relationship between the alteration layer and the dissolution rate, we developed a spatially resolved surface kinetic model for olivine dissolution and applied it to a series of closed-system experiments consisting of three-phases (water (±NaCl), olivine, and supercritical CO_2) at conditions relevant to *in situ* mineral carbonation (*i.e.* 60 °C, 100 bar CO_2). We also measured the corresponding $\delta^{26/24}$Mg of the dissolved Mg during early stages of dissolution. Analysis of the solid reaction products indicates the formation of Mg-depleted layers on the olivine surface as quickly as 2 days after the experiment was started and before the bulk solution reached saturation with respect to amorphous silica. The $\delta^{26/24}$Mg of the dissolved Mg decreased by approximately 0.4‰ in the first stages of the experiment and then approached the value of the initial olivine (−0.35‰) as the steady-state dissolution rate was approached. We attribute the preferential release of ^{24}Mg to a kinetic effect associated with the formation of a Mg-depleted layer that develops as protons exchange for Mg^{2+}.

We used experimental data to calibrate a surface kinetic model for olivine dissolution that includes crystalline olivine, a distinct "active layer" from which Mg can be preferentially removed, and secondary amorphous silica precipitation. By coupling the spatial arrangement of ions with the kinetics, this model is able to reproduce both the early and steady-state long-term dissolution rates, and the kinetic isotope fractionation. In the early stages of olivine dissolution the overall dissolution rate is controlled by exchange of protons for Mg, while the steady-state dissolution rate is controlled by the net removal of both Mg and Si from the active layer. Modeling results further indicate the importance of the spatial coupling of individual reactions that occur during olivine dissolution. The inclusion of Mg isotopes in this study demonstrates the utility of using isotopic variations to constrain interfacial mass transfer processes. Alternative kinetic frameworks, such as the one presented here, may provide new approaches for modeling fluid–rock interactions.

1. INTRODUCTION

The mineral olivine (*i.e.* $(Mg, Fe)_2SiO_4$), common in lower crustal and upper mantle rocks, is one of the most reactive rock-forming silicate minerals under surface and

* Corresponding author.
E-mail address: kmaher@stanford.edu (K. Maher).
[1] Now at: Department of Environmental Science, Policy, and Management, UC Berkeley, CA 94720, USA.

http://dx.doi.org/10.1016/j.gca.2015.11.019
0016-7037/

near surface conditions. As a result, the dissolution rate of olivine is linked to the evolution of the lithosphere and upper mantle (Sleep et al., 2004), the utility of olivine as an industrial feedstock for mineral carbonation (Oelkers and Cole, 2008), neutralization of acid mine drainage (Jambor et al., 2007), and geoengineering using enhanced silicate weathering (Koehler et al., 2010; Hartmann et al., 2013). Given the high reactivity of olivine, the surface chemistry and dissolution kinetics have been studied under a broad range of experimental conditions, including closed-system (Giammar et al., 2005; King et al., 2010; Daval et al., 2011) and well-mixed flow-through dissolution experiments on powdered olivine samples (Pokrovsky and Schott, 2000b; Oelkers, 2001), as well as single crystals (Jarvis et al., 2009; Saldi et al., 2013). Characterization of the reaction products has also included a range of techniques, such as X-ray photoelectron spectroscopy (Pokrovsky and Schott, 2000a; Zakaznova-Herzog et al., 2008; Olsson et al., 2012), infrared spectroscopy (Pokrovsky and Schott, 2000a; Giammar et al., 2005; Loring et al., 2011), transmission electron microscopy (Bearat et al., 2006; Daval et al., 2011) and atomic force microscopy (King et al., 2014). Despite the range of studies focused on olivine reactivity in the presence of aqueous solutions, predictive models for olivine dissolution are subject to large uncertainties (Daval et al., 2011; Rimstidt et al., 2012). This uncertainty has been attributed to the broad range of experimental conditions (Rimstidt et al., 2012), combined with the implicit complexity of multi-step heterogeneous reactions (Lasaga and Luttge, 2004). Improved predictive models for olivine dissolution would further aid in the design of reliable strategies for both *ex situ* and *in situ* mineral carbonation. In this paper we present a spatially resolved kinetic model for olivine dissolution constrained by time-resolved elemental compositions, Mg isotope fractionation, and High-Resolution Transmission Electron Microscopy (HR-TEM) analysis.

Characterization studies of olivine surfaces from laboratory dissolution experiments (Bearat et al., 2006; Daval et al., 2011; Ruiz-Agudo et al., 2012) have observed a pervasive Mg-depleted amorphous layer on the olivine surface after exposure to water. Exploration of the olivine-fluid interface using HR-TEM or other surface-sensitive methods suggests this coating is typically less than 50 nm thick and forms rapidly (hours to days) after contact between the fluid and olivine surface (Pokrovsky and Schott, 2000a; Bearat et al., 2006; Daval et al., 2011; Ruiz-Agudo et al., 2012). However, the temporal evolution of the forsterite coating has not been explored. As a consequence, the relationship between the Mg-depleted layer and the overall mineral dissolution rate has remained unclear.

The rapid development of Mg-depleted layers on the olivine surface during dissolution is consistent with a model in which there is exchange of Mg^{2+} ions for protons, followed by repolymerization of SiO_4 tetrahedra. Several studies have also observed the olivine dissolution rate to decrease by up to two orders of magnitude as amorphous silica (SiO_2(am)) saturation is approached (Daval et al., 2011; Johnson et al., 2014), indicating that the amorphous layer moderates the flux of Mg^{2+} and Si^{4+} ions from the olivine surface to the bulk solution. Based in part on the sharp interface between the fresh crystal and the surface layer, other studies have suggested that such coatings (which are observed on the surfaces of many silicate minerals during dissolution) are a consequence of a dissolution–reprecipitation process that does not hinder release of ions from the surface (Hellmann et al., 2012). These different observations suggest that the spatial relationship among reactions involving Mg and Si may play a role in determining the net olivine dissolution rate, and result in the orders of magnitude variability in rates observed experimentally. However, current models do not commonly address such spatial considerations, and most quantitative models do not explicitly consider the multi-step nature of the dissolution process, suggesting the need for an alternative kinetic model for olivine dissolution.

General insights into the mechanisms associated with silicate mineral dissolution may come from isotopic studies: kinetic isotope fractionation during mineral dissolution under experimental conditions is now widely observed in laboratory studies. For example, fractionation has been noted for Mg isotopes during experimental olivine dissolution (Wimpenny et al., 2010) and for Fe isotopes during experimental hornblende (Brantley et al., 2004), mica (Kiczka et al., 2010), and goethite dissolution studies (Wiederhold et al., 2006). Such isotope effects, which are not predicted by the classical description of bulk mineral dissolution, provide constraints on the ion exchange (Brantley et al., 2001) and solid-state diffusion (Verney-Carron et al., 2011) occurring at mineral surfaces during dissolution. Accordingly, various models have been developed to explain the preferential removal of isotopes from mineral surfaces. Brantley et al. (2001, 2004) first observed Fe isotopic fractionation associated with hornblende dissolution both in the presence and absence of siderophores, whereas fractionation during goethite dissolution under the same conditions was not observed. The magnitude of Fe isotopic fractionation in these studies also varied with the degree of fluid mixing and the binding affinity of the ligand for Fe. The fractionation was attributed to a kinetic isotope effect associated with the formation of a "leached layer" at the mineral surface; however, time-resolved measurements or HR-TEM images were not available. A number of additional studies have also demonstrated isotopic fractionation during mineral dissolution (Ziegler et al., 2005; Wimpenny et al., 2010; Verney-Carron et al., 2011; Pearce et al., 2012). Such fractionation is often associated with the initial stages of mineral dissolution, before a steady state and/or stoichiometric dissolution rate is reached and the isotopic composition of the dissolved fraction returns to that of the initial solid. For example, Wimpenny et al. (2010) observed that the dissolved $\delta^{26/24}$Mg released from forsterite under flow-through conditions was approximately 0.2–0.4‰ lower than that of the initial solids, an effect which was attributed to kinetic fractionation associated with preferential exchange of ^{24}Mg during mineral dissolution. Such transient isotopic fractionation thus conveys important information about ion transport and ion attachment and detachment rates at mineral surfaces that can be used to

further constrain the interfacial processes controlling mineral dissolution.

Macroscopic descriptions of mineral dissolution and precipitation are numerous, and recent studies have extended these approaches to explain kinetic and equilibrium isotope partitioning under surface reaction-controlled conditions (DePaolo, 2011; Druhan et al., 2013). Such descriptions commonly assume that the net reaction rate is the difference between the gross forward (precipitation) and backward (dissolution) rates, where each rate is associated with a kinetic fractionation (DePaolo, 2011). Although in practice it is difficult to quantify either, the backward rate and attendant kinetic fractionation factor may be constrained by the far-from-equilibrium dissolution rate (DePaolo, 2011). However, according to macroscopic descriptions, persistent kinetic isotope effects during dissolution cannot be quantified because the surface layers are removed stoichiometrically when a single net rate constant and surface area are imposed. "Ion-by-ion" models provide a microscopic description of growth kinetics and isotope and trace element partitioning based on quasi-elementary ion attachment and detachment events (Nielsen et al., 2012, 2013; Watkins et al., 2013). We use a similar surface kinetic approach here to develop a model that links the processes at the olivine interface to the macroscopic behavior indicated by the net dissolution rate. Because the individual ions (*i.e.* Mg^{2+}, Si^{4+}, and H^{+}) are evaluated independently, but coupled via spatial and stoichiometric considerations, the approach provides an alternative description of mineral dissolution and the attendant kinetic isotope fractionation that is consistent with both microscopic (HR-TEM) and macroscopic (time resolved fluid compositions) observations.

To develop this framework, we present Mg isotope data for previously published closed-system olivine dissolution experiments conducted at 60 °C, 100 bar CO_2, with solution compositions and rates detailed in Johnson et al. (2014). We also conducted a complementary suite of closed-system experiments in the presence or absence of fluid mixing and characterized the reacted olivine surfaces using HR-TEM. To explain the results from the eight experiments, a spatially resolved surface kinetic modeling approach is presented as an alternative framework for describing forsterite (Mg_2SiO_4) dissolution kinetics. This model reproduces the time-resolved solution compositions, the observed isotopic fractionation, and the general surface structure and composition.

2. METHODS

In this study we use the experimental run products (*i.e.* reacted olivine grains and resulting fluid samples) and experimental data (*i.e.* measured Mg and Si concentrations, alkalinity, and dissolved inorganic carbon, and calculated pH, saturation states and dissolution rates) from two sets of closed-system olivine dissolution experiments conducted at 60 °C and 100 bar CO_2 and detailed in Johnson et al. (2014). A brief description of these experiments and the results is presented below. We also report the $\delta^{26}Mg$ of the experimental olivine and the dissolved Mg over the duration of one short-term experiment from Johnson et al. (2014).

2.1. Olivine dissolution experiments

The experiments detailed in Johnson et al. (2014) and this study (Table 1) were conducted in a flexible and inert Au-bag reaction vessel design with modifications for sampling and analysis of CO_2 (Rosenbauer et al., 2005; Johnson et al., 2014). Reactants were placed inside the Au cell (DI water, 0.5 M NaCl, 75–105 μm forsterite at a 50:1 solution:mineral ratio by mass, or 11,470 m^{-1} in terms of surface area:volume), which was sealed and placed inside the steel autoclave and the annular space filled with DI water. After sealing the vessel, the autoclave was placed inside a rocking furnace and heated to 60 °C (Rosenbauer et al., 1983). Once this temperature was achieved, the pressure was increased to 100 bar by injection of liquid CO_2. The volume of injected CO_2 as calculated at reaction conditions (60 °C, 100 bar) was 1/10 the volume of the aqueous phase in addition to sufficient CO_2 to saturate the aqueous phase at reaction conditions (Duan and Sun, 2003; Li and Duan, 2007) and maintain a supercritical CO_2 ($scCO_2$) phase. See Johnson et al. (2014) for a more detailed description of the experimental system. Serial samples were obtained throughout each experiment. The olivine sample is (Fo92) from the Twin Sisters Dunite, Washington, USA. The olivine was prepared by repeated washes in methanol between sieving to minimize leaching

Table 1
Summary of experiments from Johnson et al. (2014) and this study used in model development.

Experiment Name	Temp. (°C)	PCO_2 (bars)	Duration (days)	Electrolyte	Mixing	Mg isotopes
Experiment 1[a]	60	100	74	0.5 M NaCl	Well-mixed	
Experiment 2[a]	60	100	92	0.5 M NaCl	Well-mixed	
Experiment 3[a]	60	100	4	None	Well-mixed	Yes
Experiment 4[a]	60	100	98	None	Well-mixed	
2-Rocking (2R)[b]	60	100	2	0.5 M NaCl	Well-mixed	
19-Rocking (19R)[b]	60	100	19	0.5 M NaCl	Well-mixed	
2-Stationary (2S) [b]	60	100	2	0.5 M NaCl	Not mixed	
19-Stationary (19S)[b]	60	100	19	0.5 M NaCl	Not mixed	

[a] Presented in Johnson et al. (2014).
[b] This study.

the surface of Mg prior to starting the experiments. The experimental olivine contains less than 3 wt.% lizardite (a serpentine-group mineral) as determined by X-ray powder diffraction. However, because the dissolution rate of lizardite is nearly three orders of magnitude slower than olivine (Daval et al., 2013), the small amount of lizardite is unlikely to contribute appreciable Mg to solution compared to olivine dissolution. The BET surface areas of experimental powders are 0.64 m^2/g for experiments 1–4 (38–75 μm) from Johnson et al. (2014) and 0.57 m^2/g (70–105 μm) for experiments 2R, 19R, and 19S for this study. For the latter series of experiments, a larger grain size was used to facilitate characterization of the olivine surface after reaction. The BET surface areas are used in the subsequent calculations.

Aqueous samples were removed from the reactor at regular intervals throughout the duration of each experiment and were analyzed for alkalinity, elemental concentration, and dissolved CO_2 concentration. Complete aqueous sampling procedures are presented in Johnson et al. (2014). Briefly, fluid compositions were measured by inductively coupled plasma optical emission spectroscopy (ICP-OES). Alkalinity measurements were made via titration with 0.16 N sulfuric acid, and dissolved CO_2 concentrations were measured using coulometry (phosphoric acid digestion followed by electrochemical analysis of released CO_2 gas). Hydrogen concentrations in the CO_2 phase were also measured for one experiment to better constrain the redox state. The combination of these measurements plus calculated equilibrium constants allowed for pH calculation (Li and Duan, 2007). The uncertainty of ICP measurements is ±10%. Standard states adopted here are: unit activity for pure minerals, unit activity of pure H_2O, unit activity of aqueous species in a hypothetical one molal solution referenced to infinite dilution, and unit fugacity of pure gases at 1 bar and 25 °C. Speciation and pH calculations were completed using the software package PHREEQC (Parkhurst and Appelo, 1999), and the included llnl.dat database, which is derived from the EQ3/EQ6 database (Wolery et al., 1990). The database was modified using CO_2 solubility and equilibrium constants for the carbonate system from Li and Duan (2007). We calculate the saturation state for relevant reactions as log (Q/K), where Q is the calculated activity product and K is the equilibrium constant.

The results of the previous experiments of Johnson et al. (2014) are presented in the present paper, all using the same starting material (Fo92 olivine), temperature (60 °C), CO_2 pressure (100 bar), and water:rock ratio by mass (50:1) as summarized in Table 1. Six experiments contained 0.5 M NaCl, whereas two had no added electrolyte. Four additional experiments were conducted to assess the temporal evolution of the olivine surface under well-mixed (continuous rocking of the experimental vessel at 8 rotations/min) and poorly mixed (stationary experimental vessel) conditions. The reacted forsterite grains were characterized by HR-TEM. The duration of the experiments ranged from 2 to 94 days. The shortest experiments were conducted with higher sampling frequency to look at the initial (non-steady state) dissolution kinetics as silica saturation is approached.

2.2. Mg isotope analyses

We analyzed the isotopic composition of the starting olivine material and the dissolved Mg from one experiment: experiment 3 (4 days, no electrolyte). For the long-term experiments, the sample volumes were small in order to maintain approximately constant water:rock ratios over more than 90 days. Thus, most of the early samples for experiments 1, 2, 4, 2R, 19R, 19S were consumed for elemental, alkalinity, dissolved inorganic carbon (DIC), and other isotopic analyses.

2.2.1. Sample preparation and chromatographic methods

All sample preparation procedures were carried out in laminar flow hoods in the PicoTrace metal-free clean laboratory at Stanford University, and all acids were Optima grade diluted with Milli-Q (18 MΩ) water. Both San Carlos, AZ olivine and the experimental olivine (WA) derived from the Twin Sisters Dunite (50 μg) were dissolved in capped screw-top Teflon beakers with 1 ml of a 3:1 mixture of concentrated HF and HNO_3, and left overnight at room temperature. The beakers were then heated to approximately 90 °C for 24 h before the caps were removed, and the HF–HNO_3 mixture was evaporated. The samples were then dissolved in 1 ml of aqua regia, left overnight at room temperature, and then evaporated to dryness and finally dissolved in 1 N HNO_3 prior to cation exchange chromatography. Fluid samples were centrifuged for 10 min, evaporated to dryness, and dissolved in 1 N HNO_3 prior to cation exchange chromatography.

To purify and isolate Mg for isotopic analysis, Mg dissolved in 1 N HNO_3 was loaded onto 0.5 ml of pre-cleaned Bio-Rad AG50W-X12 (200–400 mesh) resin. Matrix elements were eluted in 1 N HNO_3 and 0.1 N HF. Magnesium was eluted in 1 N HNO_3. The samples were then dried and the above procedure was repeated twice. Calcium was removed from the sample using Eichrom DGA resin (50–100 μm). Following the steps outlined above, the samples were dissolved in 2 N HNO_3 and loaded onto columns containing 0.2 ml of pre-cleaned Eichrom DGA resin. Mg was eluted and collected with 2 N HNO_3 while Ca remained on the columns. The collected samples were then evaporated to dryness to complete the Mg separation process. The yield on the chromatographic procedure was >99.95%. Processing of the pure Mg standards CAM1 and SU1 (internal elemental standard) with this technique did not lead to a detectable shift in the measured Mg isotope ratio.

2.2.2. MC-ICP-MS analysis

Magnesium isotope measurements were carried out on a Nu Plasma MC-ICP-MS using medium resolution and wet plasma at Stanford University. Purified Mg samples were dissolved in 2% HNO_3, centrifuged, and diluted to approximately 1.7 ppm prior to MC-ICP-MS analysis, corresponding to ca. 7.7 V ^{24}Mg/ppm. Purified Mg-bearing solution was introduced to the instrument through a self-aspirating Glass Expansion SeaSpray nebulizer directly into the spray chamber. Mg isotopes were measured simultaneously with ^{24}Mg, ^{25}Mg, and ^{26}Mg collected in the L10, L5,

and H1 Faraday cups, respectively; ion beams were positioned such that measurements were collected on the low-mass side of the CN^+ interference. Sample measurements were bracketed by analysis of the standard DSM3, and between all measurements a 2% HNO_3 rinse solution was aspirated for approximately two minutes until the signal on the H1 Faraday cup was less than 1×10^{-4} V (Galy et al., 2003). For each analysis, $\delta(^{26/24}Mg)_{DSM3}$/‰ (and $\delta(^{25/24}Mg)_{DSM3}$/‰) values were calculated by comparing the measured $^{26}Mg/^{24}Mg$ ($^{25}Mg/^{24}Mg$) ratio of the samples to the average $^{26}Mg/^{24}Mg$ ($^{25}Mg/^{24}Mg$) of the bracketing measurement standards. Hereafter, we abbreviate the $\delta(^{26/24}Mg)_{DSM3}$/‰ as the $\delta^{26}Mg$. Each sample reported in Table 2 was measured 3–7 times during different analytical sessions, and the average values and standard deviations are reported along with the number (n) of times that an individual sample was analyzed. Because of the small volume of samples, duplicate samples of experiments could not be prepared and thus the reported uncertainties reflect only the measurement uncertainty.

To constrain the accuracy and precision of measurements made on the MC-ICP-MS, we compared the measured isotope ratios at two standard deviations (2 s.d.) of pure Mg and natural rock reference materials to accepted or reported values (Table 2). The reference material CAM1 was repeatedly measured over four months of analytical sessions with a $\delta^{26}Mg$ value of -2.60 ± 0.17 ($n = 32$), in agreement with the accepted value of -2.58 ± 0.14 (Galy et al., 2003). The isotopic ratio of an in-house Mg elemental reference solution obtained from High-Purity Standards was characterized by repeated measurements over four months. This measurement standard, "Stanford University 1" (SU1) was analyzed 76 times and found to have a $\delta^{26}Mg$ value of -0.55 ± 0.14 ($n = 76$).

The $\delta^{26}Mg$ values we obtained for natural rock standards BHVO-1, BIR-1, and San Carlos olivine were also within the uncertainty of accepted values. The measured $\delta^{26}Mg$ of BHVO-1 was -0.19 ± 0.09 ($n = 7$) within the previously reported values of -0.3 ± 0.08 (Huang et al., 2009) and -0.085 (Baker et al., 2005). Measured $\delta^{26}Mg$ of BIR-1 was -0.25 ± 0.03 ($n = 2$), which is consistent with the value of -0.23 ± 0.23 (Wombacher et al., 2009) and -0.29 (Baker et al., 2005). Measured San Carlos olivine $\delta^{26}Mg$ was -0.75 ± 0.09 ($n = 5$), in agreement with other reported values of -0.73 ± 0.06 (Teng et al., 2007), within the wide range of values reported for San Carlos olivine and supporting the possibility that San Carlos olivine may reflect low-temperature hydrothermal alteration (Handler et al., 2009). In all cases, the measured $\delta^{26}Mg$ values were within the uncertainty of the literature values.

2.3. Transmission electron microscopy sample preparation and analysis

Transmission electron microscopy (TEM) samples were prepared using a Helios NanoLab 600i DualBeam Focused Ion Beam/Scanning Electron Microscope (FIB/SEM) by FEI, equipped with a Ga^+ ion beam in addition to an electron beam. Reacted forsterite samples from experiments 2R and 19R were rinsed and dried after completion of the experiment, attached to SEM mounts and plasma-coated with gold before placement inside the FIB. Unreacted forsterite was prepared in an identical manner. Once in the microscope, a flat area of at least 4×10 μm was chosen from which to cut the cross section, and the area of interest was coated with 200 nm of Pt (unreacted forsterite) or C (19R, 19S, 2R) using non-destructive electron deposition. An additional 1 μm thick coating of Pt or C was then deposited on the sample using the Ga^+ ion beam. The material deposited on the surface did not impact the imaging, as Au protected the surfaces of all samples before deposition of Pt or C. Platinum was used for the initial samples, but we switched to C when it became available because it eased sample polishing with the ion beam. The combination of electron deposition followed by ion deposition successfully shielded the mineral surface from the destructive ion beam, and no Ga was detected by TEM in the samples, indicating that we did not have implantation of Ga^+ ions. Once the

Table 2
Mg isotope data for experimental olivine and experiment 3 from Johnson et al. (2014) along with average values for reference materials, where n is number of times individual sample was analyzed to obtain the average value and standard deviation.

Samples	Time (days)	[Mg] (mM)	$\delta^{26}Mg_{DSM3} \pm$ 2 s.d.	n
Exp. olivine			-0.35 ± 0.10	($n = 8$)
Exp. 3 (no NaCl)	0.04	7.36	-0.71 ± 0.21	($n = 7$)
	0.13	9.30	-0.64 ± 0.12	($n = 4$)
	0.29	10.12	-0.58 ± 0.09	($n = 3$)
	0.63	13.92	-0.52 ± 0.21	($n = 5$)
	0.96	12.40	-0.60 ± 0.14	($n = 3$)
	1.44	13.68	-0.58 ± 0.18	($n = 3$)
	2.00	16.77	-0.48 ± 0.06	($n = 3$)
	2.52	15.80	-0.47 ± 0.27	($n = 6$)
Standards				
CAM 1			-2.60 ± 0.17	($n = 32$)
BHVO-1			-0.19 ± 0.09	($n = 7$)
BIR			-0.25 ± 0.03	($n = 2$)
San Carlos olivine			-0.75 ± 0.09	($n = 5$)
SU-1			-0.55 ± 0.14	($n = 76$)

surface was protected, two large rectangles of material were removed by ion milling from the surface, leaving a 3–4 μm thick slice between them. The sample was then rotated and ion milling was used to make a U-shaped cut on the sides and bottom of the slice. An Omniprobe AutoProbe 200 *in situ* sample lift-out system was used to remove the slice from the forsterite grain and transfer it to a copper Pelco® FIB lift-out half grid for TEM samples. The slice was welded to the grid using Pt ion deposition, then polished with ion milling to a thickness of between 70 and 100 nm. The ion beam was set to an accelerating voltage of 30 kV for most of the process, but dropped to 3–5 kV for the final polishing, which reduced the thickness of the amorphized surface layer caused by the ion beam to about 5 nm (such that a 100 nm thick slice would have 90 nm of crystalline material and 5 nm of amorphous material on each side). The final polishing was completed using the "cleaning cross section" process, which is designed to minimize redeposition of material and create a flat surface for imaging by removing material one "line" at a time (where "line" thickness is determined by the width of the beam). The sample was rotated by 2.5° from the perpendicular to account for the parabolic shape of the beam and to reduce thickness differences within the sample.

TEM analysis was completed on an FEI Tecnai TEM at 200 kV and a FEI Titan TEM with spherical aberration image correction at 300 kV. Energy Dispersive Spectroscopy (EDS) line scans were collected in scanning TEM (STEM) mode using either an EDAX SUTW or Oxford SSD EDS detector. The O-Kα, Mg-Kα, Si-Kα, Fe-Kα, and Au-Lα elemental peaks were detected and EDS peak analysis was performed using TIA (Tecnai Imaging Analysis). The bulk forsterite phase at the base of each sample was used as an internal standard to extract sensitivity factors (*k*-factors) for the peaks (except for Au), allowing for quantitative analysis of the composition across the line scan. At least two deep scans (>700 nm) were performed per sample in order to determine sensitivity factors. The maximum achievable resolution was 2–5 nm between spots (sample-dependent) and each analyzed spot had a radius of less than 1 nm. A higher spot density resulted in artificially low Mg/Si due to beam damage, as Mg migrated away from the beam. Several steps were taken to mitigate this thermally induced migration, including short collection times (0.1 s), larger step sizes (5 nm), and tuning of the beam to reduce its intensity. Beam and scan settings were verified by running EDS scans parallel to the interface and determining that the chemical composition remained constant as expected.

Visual inspection demonstrated a high level of uniformity across each 10 μm cross section. For all samples analyzed, multiple TEM images were taken of each cross section and multiple EDS line scans were performed. Each TEM image shown is representative of the forsterite surface from that sample. TEM images and EDS line scans were taken from the same cross section but not from the same location on each cross section. The EDS profiles presented for unreacted forsterite are the sum of two line scans, 2R is the sum of 5 line scans, and that for 19R reflects a single scan that was representative of other line scans collected. Given the low counts associated with very short collection times (required to prevent loss of Mg) and the possibility for artificial compositional gradients, we focus on the large-scale changes in composition and crystallinity rather than the observed chemical gradients.

An Inverse Fast Fourier Transform (IFFT) analysis was performed on TEM images to clarify which regions were crystalline and which were amorphous using ImageJ software (Rasband, 1997). The first step is to take a Fourier Transform of the image of interest, which produces another image in the frequency domain. Bright spots in the Fourier Transform image are representative of periodic regions in the original image. The frequencies of the spots were selected to pass the filter, while all other frequencies were masked, and an inverse Fourier Transform was performed. The result of this procedure is an image similar to the original, but shows only the periodic regions as a series of regular stripes. The IFFT image was used to differentiate amorphous and crystalline regions on the original image. See the Supplementary material (Fig. S1) for a diagram of this process.

3. RESULTS

3.1. Elemental concentrations and Mg isotope results

The evolution of Mg and Si concentrations and pH over time for the well-mixed experiments 1 and 2 (with 0.5 M NaCl) and experiments 3 and 4 (no NaCl) is summarized from Johnson et al. (2014) and shown in Fig. 1A–C. Early experimental stages (ca. <10 h) are characterized by incongruent dissolution with preferential release of Mg over Si. At longer times, the Mg release rate is constant while Si concentrations plateau due to precipitation of SiO_2(am) (Johnson et al., 2014). Magnesite saturation was reached between 30 and 40 days in the experiments with NaCl (experiments 1 and 2) and at 90 days in the absence of NaCl (experiment 4), although magnesite precipitation did not occur in any observable amount until after about 75 days in the NaCl experiments (Johnson et al., 2014). The alkalinity increased over the duration of each experiment in stoichiometric relation to the amount of olivine dissolution. Early and long-term rates are markedly different between the experiments with and without 0.5 M NaCl.

The second series of experiments (*i.e.* well-mixed experiments 2R and 19R, and unmixed experiment 2S and 19S, all with 0.5 M NaCl) are shown in Fig. 1D and E (concentration data and calculated saturation states are provided in Table S1). These experiments were conducted over shorter durations to examine the evolution of the altered surface layers under both well-mixed and un-mixed conditions at much slower rates. Experiment 19R released the most Mg – three times more than experiment 19S. Magnesium release from experiment 2R closely tracked that of experiment 19R over the shorter time periods of experiment 2R, indicating reproducibility of these two experiments (Fig. 1D). Experiments 2S and 19S, both of which were unmixed, show a similar evolution to the well-mixed experiments, but with lower Mg concentrations. Silicon also increased initially in all four experiments, although experiment 19R reached

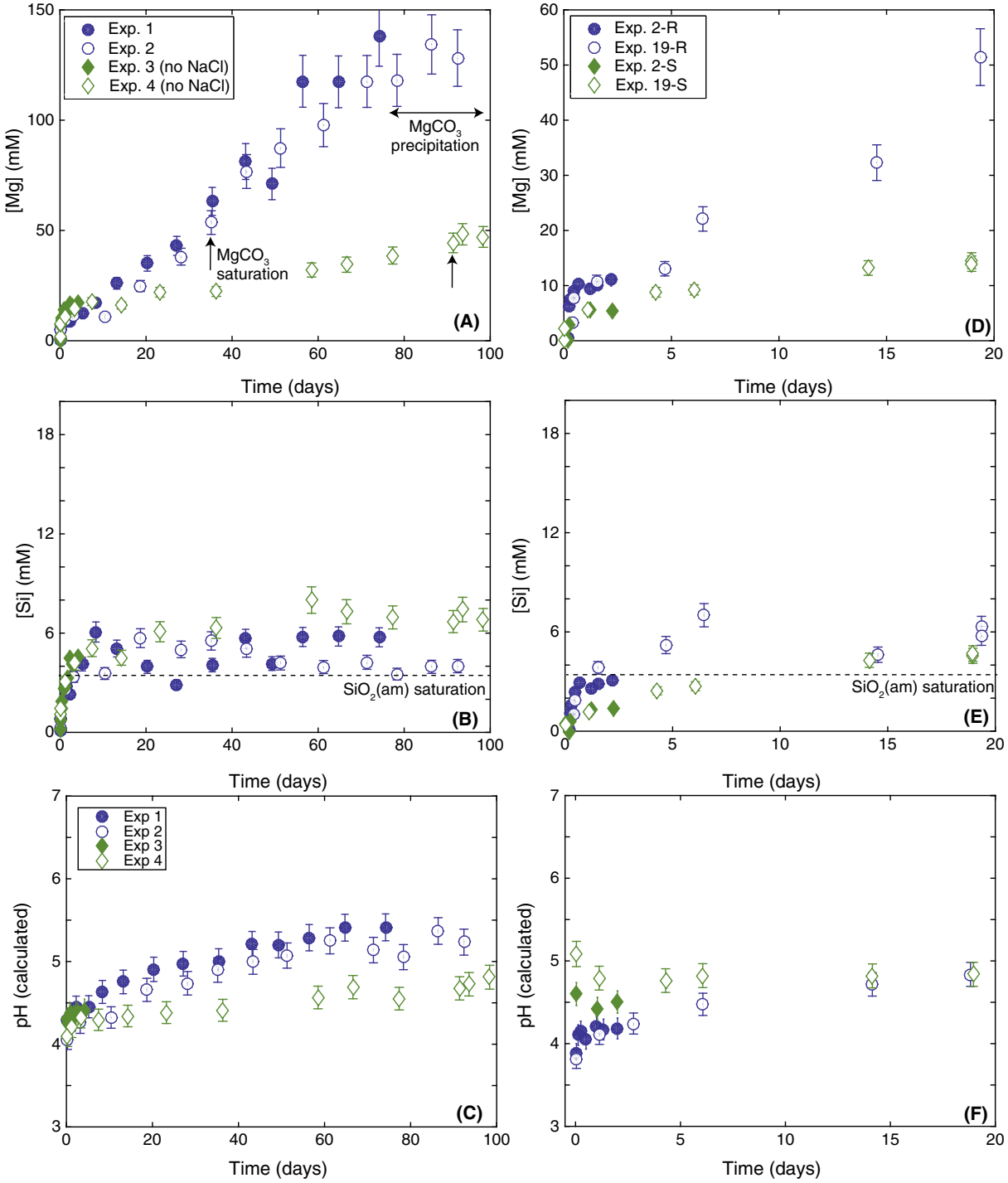

Fig. 1. Summary of previous experimental data from Johnson et al. (2014) in (A)–(C) and this study in (D)–(E). Vertical arrows in (A) and (D) indicate time when experiments reached $MgCO_3$ saturation, horizontal line with arrows indicates interval when $MgCO_3$ precipitation is thought to have occurred in experiment 2, based on the lack of precipitates in experiment 1 at 74 days. Horizontal dashed lines in (B) and (E) indicate saturation with respect to amorphous silica in a 0.5 M NaCl solution at pH 4.5. Experimental conditions are summarized in Table 1. Error bars represent 1 s.d.

a maximum concentration at 6 days (Fig. 1E). Both rocking experiments (2R and 19R) showed a trend of increasing pH with time, in contrast to the stationary experiment 19S, which showed decreasing pH over the first day (Fig. 1F).

Experiments 19R and 19S exceeded amorphous silica saturation at 2 days and 14 days, respectively, but 2R did not reach saturation (Table S1). All experiments remained undersaturated with respect to magnesite (Table S1) and

were undersaturated with respect to other likely secondary phases over their duration. For example, the saturation state for talc in 19R, defined as log (Q/K), varied from −14.0 initially to −3.7 by the end of the experiment, and similarly, the log (Q/K) for brucite varied from −9.3 to −6.6. Based on these calculations, prior SEM investigation of similar experiments in Johnson et al. (2014), and observed SiO_2(am) precipitation on a chromite grain in 19R (not shown), we infer that SiO_2(am) is the primary secondary phase. Measurements of H_2 in the $scCO_2$ phase of an experiment with a similar progression to 19S ranged from 10^{-4} to 10^{-3} bars. Accordingly, speciation calculations using PHREEQC suggest the predominant iron species in solution was ferrous.

All experiments demonstrate incongruent dissolution initially, with Mg/Si ratios decreasing from values between 4 and 6 over the first 2 days of reaction and prior to reaching saturation with respect to SiO_2(am). At longer experimental times in the well-mixed experiments 19R, the Mg/Si ratio increased with time, presumably reflecting precipitation of SiO_2(am). In contrast, the Mg/Si ratio of 19S appears to stabilize at a value of about 3.1, indicating minimal amounts of Mg release at late stages in the experiment.

Results of Mg isotopic measurement of WA olivine and the samples from experiment 3 are presented in Table 2. All fluid samples from experiment 3 were isotopically enriched in ^{24}Mg ($\delta^{26}Mg$ from −0.71 to −0.47) compared to WA Olivine ($\delta^{26}Mg$ of −0.35). The $\delta^{26}Mg$ of the first fluid sample has the lowest $\delta^{26}Mg$ value, and as the experiment progressed the dissolved $\delta^{26}Mg$ values increased progressively such that the $\delta^{26}Mg$ of the final sample is within uncertainty of the value of unreacted WA Olivine (Fig. 2). The Mg isotopic measurements of samples from experiment 3 are consistent with the preferential release of ^{24}Mg during olivine dissolution, and in agreement with prior results from flow-through experiments (Wimpenny et al., 2010).

3.2. Transmission electron microscopy

Complementary HR-TEM analyses after 2 and 19 days of reaction constrain the evolution of the thickness of the altered surface layers (Fig. 3). Unreacted forsterite (Fig. 3A) does not show an amorphous region at the mineral surface, whereas an amorphous layer of thickness 10–25 nm is visible after 2 days of reaction (Fig. 3B). The amorphous-crystalline interface on sample 2R is complex may be characterized as an altered layer with regions of both amorphous and crystalline material. However, after 19 days of reaction more homogeneous amorphous layers of thicknesses 65–71 nm (19R) and 35–43 nm are apparent from 19S (Fig. 3C). In all reacted samples, some of the gold coating appears to have penetrated the surface layer and deposited inside pores, as evidenced by the darker spots inside the amorphous regions. No gold penetrated the surface of the unreacted olivine, suggesting that the gold visible in the reacted samples is the result of porosity and not due to destructive deposition. Inspection of TEM images of larger areas (at lower zoom levels) and from two cross-sections from two different mineral grains from sample 19R indicated the uniformity of the surface layer (not shown). Although the lattice spacing suggests different forsterite crystal faces are present, we do not see a strong relationship between the thickness of the surface layer and the particular orientation of the surface layer, in contrast with previous work for both olivine (King et al., 2014) and diopside (Daval et al., 2013). These results suggest that images we present are broadly representative of features associated

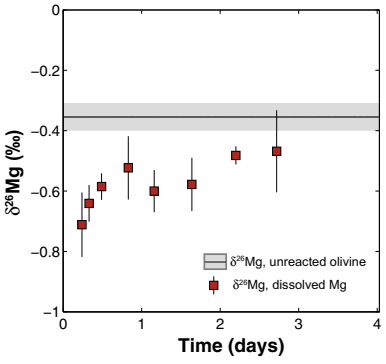

Fig. 2. Magnesium isotope data for the short-term experiment 3 (no NaCl) over 3 days of reaction time. Error bars represent 1 s.d.

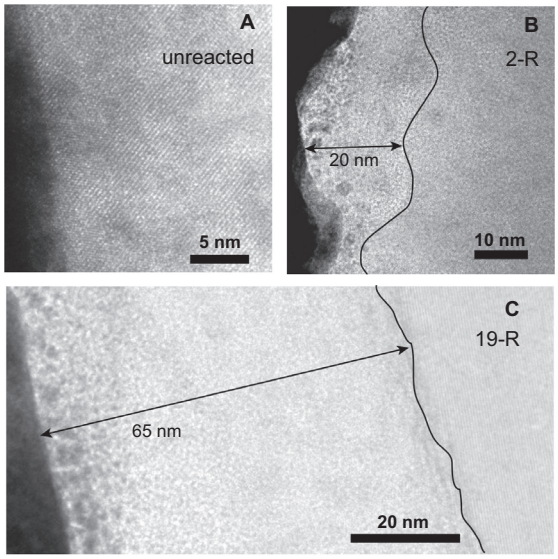

Fig. 3. High-resolution TEM images of the solid-aqueous interfaces for (A) unreacted forsterite, (B) 2R and (C) 19R. In the unreacted sample, lattice fringes extend to the mineral surface, indicating the absence of an amorphous surface layer. Images from experiment 2R (B) and 19R (C) show the entire thickness of the surface layer, with the left side bounded by a protective coating of gold (black material, deposited after reaction) and roughly vertical lines overlaid to show the transition from amorphous to crystalline material. Magnification of the amorphous-crystalline interface shows that it is less than 5 nm in thickness in 19R (Fig. S1). Lines indicate the transitions from crystalline domains to amorphous domains according to IFFT results (Fig. S1). Gold coating applied to protect the surface during imaging and cross-section preparation is clearly visible as dark material on the left side of five of the TEM images. Amorphous regions are located to the left of the black lines.

with the reacted forsterite surface under the given conditions.

In all samples, the EDS results suggest multiple chemical gradients indicating interfaces of finite thickness (Fig. S2). Such gradients could be attributed to beam damage, redeposition during the ion milling process, or sample orientation; hence, the EDS results cannot be definitively associated with compositional gradients but can be used as additional mass balance constraints in the modeling approach described below. For example, the EDS results indicate compositional differences among the amorphous regions of the interface (Mg/Si < 1.84) compared to the crystalline olivine (Mg/Si ~ 1.84). Values of Mg/Si between 1.2 and 1.5 are characteristic of the amorphous regions closest to the crystalline forsterite and values of <0.5 are typical of the outermost amorphous regions. No distinct features are visible in the Fe/Si ratios in any of the surface layers. However, Fe signals from all samples were quite low due to the low beam intensity needed to accurately collect Mg data, and thus the Fe/Si ratios will not be discussed further.

4. DISCUSSION

4.1. Conceptual framework and spatial considerations for olivine dissolution

The experimental results considered here represent an array of conditions likely to occur as CO_2-rich fluids react with lithologies rich in olivine. The first set of experiments detailed in Johnson et al. (2014) (experiments 1–4) considered the effect of supporting electrolyte and found that in the presence of 0.5 M NaCl the initial olivine dissolution rates were slower, whereas the long-term rates were more rapid, compared to the experiments with no electrolyte in the initial solution. Here we present new δ^{26}Mg data for the electrolyte-free experiment. The second set of experiments (2R, 2S, 19R, 19S) compares the effects of well-mixed and un-mixed conditions. In the mixed experiments, dissolution rates were approximately five times faster compared to the un-mixed experiments. Cross-sections of unreacted and reacted olivine grains after 2 and 19 days of reaction were also analyzed for crystallinity and chemical composition using HR-TEM as summarized in Fig. 4. A complex sequence of Mg-depleted surface layers is observed: (1) crystalline olivine, (2) an amorphous "active layer" (*AL*) where Mg/Si decreases rapidly towards the solid-solution interface, and (3) a newly precipitated amorphous layer where Mg/Si < 0.5 in 19R (Fig. 4). The active layer was present and of a similar thickness on all reacted forsterite grains. In contrast, the precipitated layer was only visible in experiments that exceeded SiO_2(am) saturation. Given the constant release rate of Mg and the 20–40% porosity observed in TEM images (quantified by comparing the darkened areas (gold) to the total area of material), the precipitated layer does not form an appreciable barrier to ion transport from the active layer to the bulk fluid.

The entire sequence of alteration is consistent with both the development of a non-stoichiometric "leached layer" (e.g., Luce et al., 1972; Schott et al., 1981; Chou and Wollast, 1984; Casey et al., 1988; Casey and Bunker, 1990; Stillings and Brantley, 1995; Hellmann, 1997; Pokrovsky and Schott, 2000a,b; Schott et al., 2012), and a process of interfacial dissolution–reprecipitation (Putnis, 2009; King et al., 2010; Hellmann et al., 2012; King et al., 2014; Ruiz-Agudo et al., 2014). However, given the stratigraphy evident in the alteration layer, including a sharp transition between amorphous and crystalline material and distinct compositional differences indicated by the Mg/Si profiles, we subdivide the altered layer into the zones defined above and in Fig. 4 in the development of the kinetic model. First, we assume an average value for Mg/Si within the active layer that evolves from an initial stoichiometric value to the value required by mass balance constraints imposed by time-resolved solution compositions and the HR-TEM profiles (Fig. 4C). If Mg release is kinetically controlled, the initial development of the active layer should preferentially contribute ^{24}Mg to solution, resulting in lower dissolved δ^{26}Mg relative to the bulk olivine as observed. Second, we do not explicitly treat the process of solid-state diffusion (e.g., Yang et al., 2009; Hellmann et al., 2012). Instead, we assume a stoichiometric flux of Si and Mg into the active layer and account for the total Mg depletion within the active layer. The consequences of these assumptions will be discussed in Section 4.3.2. Conceptually, the active layer can be viewed as a reaction front that maintains a constant thickness as it advances into the unreacted olivine (Hellmann et al., 2012). This thickness is moderated by the balance between the removal of ions at the fluid-active layer interface and the supply of ions from the crystalline olivine.

In summary, the key features of olivine dissolution we seek to address through development of an alternative kinetic model include: (1) non-stoichiometric release of Mg relative to Si during the early stages (ca. <1 day of reaction time); (2) enhancement of the Mg release rate at early times in the absence of an electrolyte, followed by lower steady-state dissolution rates compared to experiments with an electrolyte present, (3) preferential release of ^{24}Mg to solution during the early stages, (4) dependence of the dissolution rate on pH, and (5) a zone of Mg depletion between the fluid–solid interface and the crystalline olivine. To capture these processes and features, we have developed a framework that considers the exchange of individual ions within the active layer and between the surface of the active layer and the bulk solution, and builds upon numerous previous models (e.g., Pokrovsky and Schott, 2000a,b; Daval et al., 2011; Rimstidt et al., 2012).

4.2. Spatially resolved surface kinetic model for olivine dissolution

4.2.1. Stoichiometric and mass balance constraints

For olivine, where octahedrally coordinated Mg is linked to isolated silicate tetrahedra, protonation of the magnesium surface sites is required to release magnesium from the bulk crystal and maintain charge neutrality (for clarity, Fe is omitted below). The hydrolysis reaction requires the exchange of four protons for two magnesium ions at the surface of the mineral, followed by

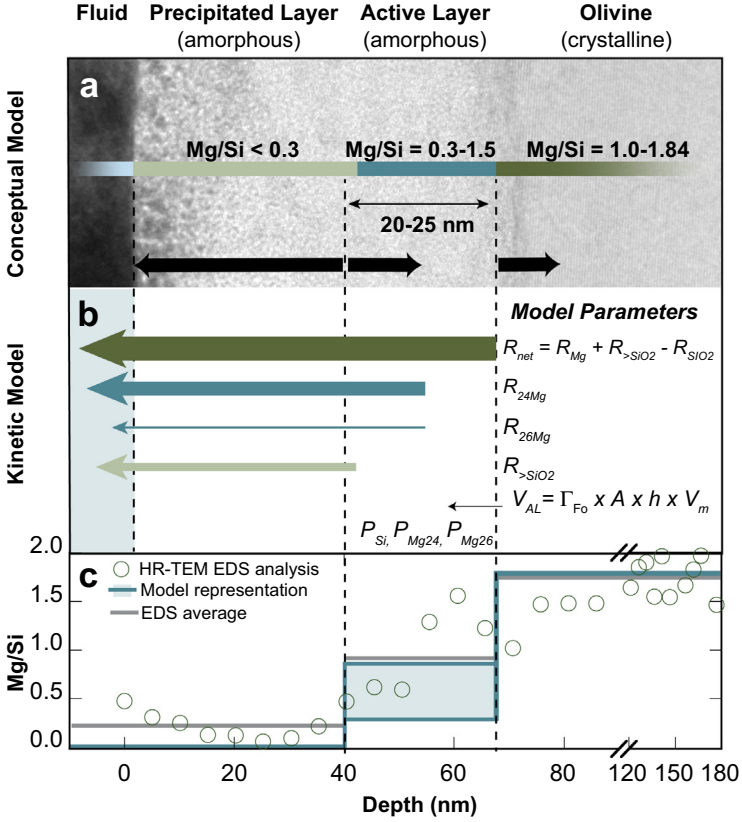

Fig. 4. Conceptual model for the spatially resolved surface kinetic model. (A) High resolution TEM image shows the general features observed in the outer 100 nm of olivine after reaction for 19 days, with the fluid–solid interface to the left of the image. Average Mg/Si ratios measured by EDS are provided for reference (the Mg/Si of 1.84, the O/Si of 4, and Fe/Si of 0.16 for pristine unreacted olivine agree with previous electron microprobe analyses reported in Johnson et al. (2014)). The black arrows indicate the migration of the active layer into the crystalline olivine over time, as determined by the rates of the individual reactions in (B). (B) The conceptual model for the independent rates considered in the model (see text for parameters) and the resulting mass balance constraints. The net rate (R_{net}) is the Mg exchange rate plus the net difference between the net $<SiO_2$ dissolution rate and the net precipitation rate of amorphous silica (when relevant). Magnesium is removed from the active layer of volume V_{AL}, while $>SiO_2$ can only be dissolved or added from the surface of the active layer. (C) Representative HR-TEM EDS linescan of the Mg/Si ratio in reacted olivine from experiment 19R showing average values (gray line) compared to the model representation (blue line, shaded region indicates range). Note the break in scale at 80 nm. (For interpretation of the references to color in this figure legend, the reader is referred to the web version of this article.)

polymerization of the isolated surface silicate tetrahedra (Pokrovsky and Schott, 2000b), according to the following net reaction:

$$> Mg_2SiO_4 + 4H^+ \longrightarrow > SiO_2 + 2H_2O + 2Mg^{2+} \quad (1)$$

where $>$ represents a site within the active layer. At low temperatures, Reaction (1) is considered irreversible, and the rate should depend on pH (Pokrovsky and Schott, 2000a). However, the exact dependence is difficult to constrain as protons may also be distributed between surface sites and/or adsorbed to surface layers (Pokrovsky and Schott, 2000a). Diffusion of Mg out of the active layer is not the rate-controlling step for Reaction (1) under well-mixed conditions because the steady-state dissolution rate is independent of Mg concentration in solution (Pokrovsky and Schott, 2000b; Oelkers, 2001; Johnson et al., 2014).

Although Reaction (1) has been included in previous models, it has not been explicitly linked to the compositional evolution of the surface. Here, Reaction (1) only occurs within the volume (V_{AL}, m^3) of material defined as the active layer (Fig. 4B), as suggested by both the HR-TEM results and the early non-stoichiometric dissolution observed in the experiments. Penetration of protons into the olivine structure at depths greater than one unit cell is further suggested by X-ray photoelectron spectroscopy (XPS) of the olivine surface (Pokrovsky and Schott, 2000a; Johnson et al., 2014), a decrease in the apparent pH point of zero charge (pH_{PZC}) from fresh to reacted forsterite (Pokrovsky and Schott, 2000a), and depth profiles of H in reacted olivine using RNRA (Resonant Nuclear Reaction Analysis) (Petit et al., 1990). The V_{AL} is calculated as $\Gamma_{Fo}AhV_m$, where Γ_{Fo} is the site density of olivine (3.3×10^{-5} mol/m^2 Wogelius and Walther, 1991), A is the physical surface area in m^2 from measured BET surface area and the mass of initial olivine, V_m is the molar volume of olivine (4.38×10^{-5} m^3/mol) and h is the number of olivine layers from which Mg can be extracted according to Reaction (1). A list of parameters is presented in Table 3.

Table 3
Model parameters and values applied to experiments 1–4, 2R, 19S, 2S, 19S.

Parameter	Description	Units	Value or range
V_m	Molar volume forsterite	$m^3\ mol^{-1}$	4.38×10^{-5}
V_m	Molar volume SiO_2(am)	$m^3\ mol^{-1}$	2.90×10^{-5}
Γ_{Fo}	Site density	$mol\ m^{-2}\ layer^{-1}$	3.3×10^{-5}[a]
h	Number of layers	–	14[b]
A	Surface area	m^2	2.24[c]/2.0[d]
V_{AL}	Active layer volume $= \Gamma_{Fo} A\ h V_m$	m^3	Calculated
$R_{Mg,i}$	Mg isotope release rate	$mol\ s^{-1}$	Calculated
$R_{>SiO_2}$	Net SiO_2 release rate	$mol\ s^{-1}$	Calculated
$R_{SiO_{2(am)}}$	Precipitation rate	$mol\ s^{-1}$	Calculated
v_{Mg}	Exchange rate coefficient for Mg	s^{-1}	Variable
$v_{>SiO_2}$	Detachment rate coefficient for $>SiO_2$	s^{-1}	Variable
$k_{>SiO_2}$	Attachment rate coefficient for $>SiO_2$	$M^{-1}\ s^{-1}$	Variable
k_{SiO_2}	Rate coefficient for SiO_2(am)	$mol\ m^{-2}\ s^{-1}$	Variable
$X_{Mg/Fo}$	Mole fraction Mg in olivine		1.84[c]
$X_{Mg,i}$	Mole fraction of i in Mg component		Calculated
$\alpha_{Mg\text{-}Fo}$	Kinetic fractionation factor	–	Variable
P_{Mg26}, P_{Mg24}	Concentration in V_{AL}	$mol\ m^{-3}$	Calculated
$P_{>SiO_2}$	Concentration of $>SiO_2$ in V_{AL}	$mol\ m^{-3}$	Calculated
K_{SiO_2}	Equilibrium constant for SiO_2(am)	–	$10^{-2.4067}$[e]

[a] Wogelius and Walther (1991).
[b] Calculated from TEM data based on thickness of active layer from (see Supporting materials).
[c] From Johnson et al. (2014) applied to experiments 1–4.
[d] From this study, applied to experiments 2R, 19R, 19S.
[e] From SUPCRT92 thermodynamic database (Johnson et al., 1992).

The equivalent thickness of the active layer is 20 nm ($h \approx 14$) with a steady-state Mg/Si of 0.3–1.5 determined by (1) the rates required to match the measured Mg and Si release rates of Fig. 1 and (2) mass balance considerations based on HR-TEM imaging of olivine cross-sections shown conceptually in Fig. 4C.

As the active layer forms, residual silica populates the volume that was once crystalline olivine. The volume increase from crystalline olivine to amorphous silica, on a per mole basis, is approximately 33%. Although volumetric expansion mostly likely occurs during the formation of the active layer, we cannot constrain the extent. Therefore, the overall mass balance is calculated on a per mol basis so the potential volume increase does not impact the model results. Our calculation of V_{AL} based on an active layer thickness of 20 nm is consistent with a volume increase of about 30% based on the HR-TEM results. Active layer thickness is provided hereafter only as a guide.

Once the surface silica sites are formed, the dissolution of surface silica can be treated as a reversible reaction:

$$> SiO_2 + 2H_2O \rightleftharpoons H_4SiO_4(aq) \quad (2)$$

Closed-system experiments generally show a decrease in dissolution rate as Si concentrations approach SiO_2(am) saturation (Daval et al., 2011; Saldi et al., 2013; Johnson et al., 2014), consistent with Eq. (2) as a factor in the overall dissolution rate. However, after SiO_2(am) saturation is reached in experiments 1, 2, 4 and 19R, Mg concentrations continue to increase at a constant but slower rate. A similar result was observed for Fo_{90} in the batch experiments of Saldi et al. (2013). The observed dependence of overall rate on aqueous Si concentrations combined with continued dissolution once the active layer forms, suggests that removal of silica is confined to the surface of the active layer, $\Gamma_{Fo}A$, rather than occurring throughout V_{AL} (Fig. 4B). This spatial constraint is required to reproduce both the observed non-stoichiometric dissolution, and the subsequent development of a steady-state active layer thickness and dissolution rate. Mathematically, the active layer can be viewed as a reaction front that develops and moves inward at a rate controlled by both the rate of Mg exchange according to Reaction (1) and the net release of Si via Reaction (2).

Precipitation of new SiO_2(am) can occur directly on the mineral surface or in other parts of the reaction vessel as shown by Reaction (3):

$$H_4SiO_4(aq) \rightleftharpoons > SiO_2 + 2H_2O \quad (3)$$

This local equilibrium controls the aqueous Si (*i.e.* H_4SiO_4(aq)) at later stages of the experiments once SiO_2(am) saturation is exceeded (*e.g.*, Fig. 1).

Reactions (1) through (3), combined with the conceptual model of Fig. 4, emphasize the coupled reactions that occur during the initial and steady-state periods of olivine dissolution. The rate of Reaction (1) and the net rate of Reaction (2) can be considered to control the dissolution rate of olivine, while Reaction (3) represents an indirect control on both the rates of Reactions (1) and (2) at greater extents of reaction progress as it determines the aqueous Si concentrations once amorphous silica saturation is reached. Although previous models have considered such coupling (Pokrovsky and Schott, 2000b; Daval et al., 2011), the spatial relationships among the reactions have not been explicitly accounted for. We hypothesize that it is the spatial relationship among the reactions that results in a stabilizing

feedback that moderates overall dissolution rates, and explains the majority of the dissolution behavior outlined above.

Iron is also thought to play a role in the evolution of the surface layer, particularly if Fe(III)-rich silica layers form (Schott and Berner, 1983; Saldi et al., 2013; Sissmann et al., 2013). For example, in an olivine dissolution experiment conducted by Sissmann et al. (2013) gradual passivation of the olivine surface close to saturation with respect to amorphous silica was attributed to the formation of Fe(III)/Si-rich surface layer. As conditions in the reactor became more reducing, the dissolution reactions resumed presumably due to breakdown of the Fe(III)-rich passivating layer. In our experiments, based on measured H_2(gas), conditions remained reducing over the course of the experiment, lessening the impact of ferric iron. We also do not see Fe enrichment in the active or precipitated layer based on TEM-EDS analyses of the reacted interfaces. Thus, under more oxidizing conditions the model presented here would need to be amended to account for the role of Fe in passivating the forsterite surface.

4.2.2. Rate equations and inclusion of isotopes as additional constraints

Similar to the assumptions commonly made to describe mineral dissolution rates, most previous surface isotope exchange models assume the surface layer composition is at steady state (DePaolo, 2011; Nielsen et al., 2012). Here, the development of the active layer results in a surface layer that is multiple unit cells thick and evolving isotopically and compositionally through time. Such transient behavior is difficult to solve for analytically. Thus, we use a numerical model to track the fluid and solid compositions over time given the coupling among Reactions (1)–(3) enforced by the spatial constraints and the kinetic framework presented below. The approach is conceptually similar to that of Brantley et al. (2004) and Wiederhold et al. (2006). However, previous studies were not able to precisely constrain the size of the active layer, or did not require it.

In order to develop a kinetic model for the Reactions (1)–(3), that includes a provision for kinetic fractionation of Mg isotopes during the early stages of dissolution, we used a set of relationships that are based on the "ion-by-ion" growth model developed for crystal growth and applied to calcite precipitation in Nielsen et al. (2012, 2013). In this approach, the olivine dissolution rate is described by the net rate R_{net}, which is the difference between the ion fluxes from (R_b) and to (R_f) and the surface, where the subscript b refers to the backward or dissolution reaction and subscript f refers to the forward or precipitation reaction (DePaolo, 2011). As Reaction (1) is treated as irreversible, the flux of Mg is only characterized by R_b, providing an opportunity to quantify both R_b and the associated kinetic isotope effect. In contrast, Reactions (2) and (3) are assumed to be reversible and thus only the net Si release is observable.

The isotope-specific Mg exchange rate (R_{Mg}, mol/s) from the active layer associated with Reaction (1) is a function of the rate coefficient for Mg exchange, v_{Mg} (s^{-1}) and the concentration, P_i (mol/m^3) of a given isotope or solid component, i, in the surface layer:

$$R_{24Mg} = v_{Mg} a_{H+}^{n} P_{24Mg} V_{AL} \quad (4)$$

The dependence of Mg exchange rate on pH is expressed via a dependence on the proton activity ($a_{H+}{}^{n}$), where n is between 0 and 0.5 (Pokrovsky and Schott, 2000a; Rimstidt et al., 2012). The value of n is difficult to assess because of the variable mechanisms for proton uptake, so we adopt the value of 0.37 suggested by Rimstidt et al. (2012) based on synthesis of a large number of experimental studies conducted in the presence of CO_2. The n value of 0.37 is also close to the slope observed between Mg concentration and protons consumed in other studies and is assumed to reflect the combined influence of exchange and adsorption (Luce et al., 1972; Pokrovsky and Schott, 2000a). As Reaction (1) is expressed as a net reaction, the assignment of an empirical (rather than stoichiometric) value for n is required, and a sensitivity analysis of n values is shown in Fig. S3. Similarly, for the minor isotope, ^{26}Mg, the rate equation can be written in terms of the common isotope using the kinetic fractionation factor between Mg^{2+} in olivine and in solution ($\alpha_{Mg\text{-}Fo}$), to describe the preferential removal of ^{24}Mg:

$$R_{26Mg} = \alpha_{Mg\text{-}Fo} v_{Mg} a_{H+}^{n} P_{26Mg} V_{AL} \quad (5)$$

The exchange rate coefficient, v_{Mg}, along with $\alpha_{Mg\text{-}Fo}$ constitute the unknowns in the rate equations. Reaction (1) is used to represent the stoichiometry for mass balance purposes. Although we track the individual rates, V_{AL} is originally determined based on the molar volume of olivine, and hence it is equivalent to calculating the rates in terms of mole fraction and the number of original moles of olivine in the active layer. Thus, any positive volume change associated with Reaction (2) does not impact our mass balance results.

Although Mg isotopes are not required to model olivine dissolution using our approach, we demonstrate how they provide a useful constraint on the rate of Reaction (1). The model approach we present may also be useful for considering other kinetic isotopes effects (e.g., Pearce et al., 2012). However, in order to model isotopic fractionation additional provisions are required. First, we calculate P_{24Mg} initially as a function of the mole fraction of Mg that is ^{24}Mg, X_{24Mg}, and the stoichiometric Mg:Si ratio in olivine, $X_{Mg/Fo}$ (1.84 for the olivine considered here):

$$P_{24Mg}(\text{initial}) = X_{24Mg} X_{Mg/Fo} V_m^{-1} \quad (6)$$

An analogous equation describes P_{26Mg}. As the surface layer evolves, $P_{Mg,i}$ is tracked according to the individual reaction rates. In addition to the coupling between Mg and Si mole fractions in the solid associated with Reaction (1), the removal of $>SiO_2$ sites allows the reaction front to migrate inward, supplying Mg_2SiO_4 to the active layer. Thus, $P_{Mg,i}$ is not only a function of the magnesium release rate but also the net rate of Reaction (2). To describe the net rate of silica release ($R_{>SiO_2}$) from the active layer associated with Reaction (2), we assume that the backward (detachment) rate is a function of the concentration of $>SiO_2$ at the surface only, whereas the forward (attach-

ment) rate is a function of both $>SiO_2$ and the aqueous Si activity, $[H_4SiO_4]$:

$$R_{>SiO_2} = (v_{>SiO_2}P_{>SiO_2} - k_{>SiO_2}[H_4SiO_4]P_{>SiO_2})\Gamma_{Fo}AV_m \quad (7)$$

where $v_{>SiO_2}$ (s^{-1}) is the surface detachment rate and $P_{>SiO_2}$ is the concentration of Si surface sites throughout V_{AL} and $k_{>SiO_2}$ ($M^{-1}\,s^{-1}$) is the rate constant associated with attachment of SiO_2 at the surface. The key difference between Eq. (7) and Eqs. (4) and (5) is that the thickness of the surface layer is not included in this rate expression because we assume that the attachment and detachment of Si can only occur at the surface rather than from the entire volume of the active layer (*i.e.* $h = 1$). This treatment allows for incongruent dissolution during the active layer formation, and maintains a constant active layer thickness as suggested by HR-TEM analyses. Eq. (7) is computed for the Si associated with each Mg isotope. Initially $P_{>SiO_2}$ is assumed to be zero, and is sequentially updated based on the rates from Eqs. (4)–(7).

The rate of new silica precipitation is described according to the equilibrium constant for SiO_2(am), or K_{SiO_2}, and the rate coefficient k_{SiO_2} (mol $m^{-2}\,s^{-1}$):

$$R_{SiO_2(am)} = Ak_{SiO_2}\left(\frac{[H_4SiO_4]}{K_{>SiO_2}} - 1\right) \quad (8)$$

To calculate both the non-steady state evolution of the surface layer, and the spatial relationship between the ion-specific reactions, we couple the rate formulations above to the active layer concentrations (P_i) according to:

$$\frac{dP_{24Mg}}{dt} = (-R_{24Mg} + R_{>SiO_2}X_{24Mg}X_{Mg/Fo})/V_{AL} \quad (9)$$

$$\frac{dP_{26Mg}}{dt} = (-R_{26Mg} + R_{>SiO_2}X_{26Mg}X_{Mg/Fo})/V_{AL} \quad (10)$$

$$\frac{dP_{>SiO_2}}{dt} = [(R_{24Mg} + R_{26Mg})/X_{Mg/Fo} - R_{>SiO_2}]/V_{AL} \quad (11)$$

In Eqs. (9) and (10) the concentration of Mg in the active layer is determined by the balance between the rate of Mg exchange and the detachment rate of $>SiO_2$, as required to maintain the constant V_{AL} suggested by HR-TEM characterization. Similarly, the concentration of $>SiO_2$ is controlled by the difference between the rate of Mg exchange, which generates $>SiO_2$, and the net removal of $>SiO_2$ from the active layer. These equations emphasize the coupling between the Mg and Si removal rates and the distribution of Mg and Si in the altered layer.

The corresponding active layer Mg/Si $(Mg/Si)_{AL}$ can be calculated from:

$$\left(\frac{Mg}{Si}\right)_{AL}(t) = (P_{Mg})(t)/\left[\left(P_{Mg}(t)/X_{Mg/Fo}\right) + P_{>SiO_2}(t)\right]. \quad (12)$$

This approach uniquely allows us to track the Mg/Si and $\delta^{26}Mg$ in the active layer and the fluid without assuming a steady-state surface composition. We do not explicitly consider Mg isotope fractionation associated with solid-state diffusion as a potential factor given the low temperature of the experiments (Verney-Carron et al., 2011); thus any fractionation arising from more rapid diffusion of ^{24}Mg would be embedded in the calculated fractionation factor. In addition, based on HR-TEM analysis roughly 50–85% of Mg is lost from the active layer. Mg removal from the active layer may occur directly to solution followed by aqueous diffusion through open pores to bulk solution, and negligible fractionation is predicted or observed for aqueous Mg diffusion (Richter et al., 2006; Bourg et al., 2010).

The coupled set of equations represented by Eqs. (1) through (12), combined with the constraints on the active layer provided by isotopic data, HR-TEM analyses, and time-resolved solution compositions, results in the following adjustable parameters that are fit using the experimental data (1) v_{Mg} (and α_{Mg}, which depends on v_{Mg}), and (2) $v_{>SiO_2}$ and $k_{>SiO_2}$, which determine $R_{>SiO_2}$. The value of k_{SiO_2} cannot be precisely determined because we do not know the surface area associated with SiO_2(am) precipitation, although the long-term steady-state Si concentrations provide a useful constraint on the overall rate. We emphasize that the model we present, although it considers the fluxes of individual ions, is based on assumed relationships and effective fluxes.

4.3. Application of model to experimental data

To model the closed-system experimental data of Johnson et al. (2014) and this study, we use a forward model of the coupled set of Reactions/Eqs. (1)–(12) using the reactor volume, the initial mass of olivine, homogenous stoichiometric olivine with Mg/Si of 1.84, and the measured BET surface area as initial conditions (see Table 3 for parameter values and sources). We do not consider aqueous or solid state diffusion and thus rates are effective rates. Alkalinity is calculated based on the Mg release rate and is used to solve for pH according to "apparent" equilibrium constants for CO_2 solubility and carbonate speciation in the presence or absence of 0.5 M NaCl and at appropriate temperature and pressures using the model of Li and Duan (2007). We do not include a full multi-component aqueous speciation calculation (*i.e.* we assume unit activity coefficients for aqueous species). This simplification is justified because magnesite precipitation does not occur within the time frame we are modeling, and SiO_2(am) solubility is not appreciably sensitive to pH within the range of our modeling.

Because the early release rates of both Mg and Si are controlled by the rate of Reaction (1), v_{Mg} was adjusted to match the early (<~2–3 days) experimental Mg and Si profiles. Then, because the net removal of $>SiO_2$ according to Reaction (2) controls the supply of the Mg to the active layer via Eqs. (9) and (10), $R_{>SiO_2}$ is an additional control on Mg concentrations at steady state. As Si concentrations plateau once the active layer is formed due to SiO_2(am) precipitation, the early SiO_2 and long-term Mg profiles constrain the net $>SiO_2$ dissolution rate. Accordingly, by varying the ratio of $v_{>SiO_2}$ to $k_{>SiO_2}$, the overall dissolution rate was adjusted to match the long-term Mg profile. The model fit to experiments 1 and 2 is considered the "reference model" hereafter, with parameters provided in Table 4. The reference model was then adjusted to fit the additional experimental data following the above procedure. A sensitivity analysis for each model parameter is provided in Fig. S3.

Table 4
Summary of model fits to experimental data, including individual rate constants and the final rates.

Experiment name	v_{Mg} (s^{-1})	$v_{>SiO_2}$ (s^{-1})	$k_{>SiO_2}$ ($M^{-1}\ s^{-1}$)	k_{SiO_2} (mol $m^{-2}\ s^{-1}$)	Log final rate (mol $cm^{-2}\ s^{-1}$)	$\alpha_{Mg\text{-}Fo}$
Exps. 1, 2[a]	$3.0 \pm 1.5 \times 10^{-4}$	$2.9 \pm 1.4 \times 10^{-5}$	$<3.46 \times 10^{-4}$[c]	$\sim 3.3 \times 10^{-9}$	−13.13	
Exps. 3, 4[a]	$8.6 \pm 3.0 \times 10^{-4}$	$7.5 \pm 2.2 \times 10^{-5}$	$1.7 \pm 0.1 \times 10^{-2}$	$\sim 3.3 \times 10^{-9}$	−13.75	0.9993 ± 3
Exps. 2R, 19R[b]	$6 \pm 3.0 \times 10^{-4}$	$2.5 \pm 0.7 \times 10^{-5}$	$<7.3 \times 10^{-4}$[c]	$\sim 3.3 \times 10^{-9}$	−13.01	
Exps. 19S[b]	$1.0 \pm 0.5 \times 10^{-4}$	$3.8 \pm 1.3 \times 10^{-6}$	$<5.0 \times 10^{-4}$[c]	$\sim 3.3 \times 10^{-9}$	−14.03	
Wimpenny et al. (2010)[d]	2.1×10^{-4}	3.4×10^{-4}	nd	nd	−12.18	~0.999

nd: Not determined.
[a] Johnson et al. (2014), experiments conducted at 60 °C, 100 bars CO_2.
[b] This study, experiments conducted at 60 °C, 100 bars CO_2.
[c] Only the maximum possible rate could be determined for a given $v_{>SiO_2}$.
[d] Experiments conducted at 25 °C, and pH 3. The surface layer thickness used in model is 28 nm, while other parameters are from the study or provided above. Sensitivity is provided in Fig. 9.

The model is able to reproduce the major features of the data from experiments 1–4, including the initial incongruent dissolution (Fig. 5). The Mg/Si in the active layer evolves from 1.84 to 0.5 after 5 days (the isotopic and surface layer evolution will be discussed in more detail in Section 4.4). Relative to experiments 1 and 2, the early Mg release rate in the electrolyte-free experiments 3 and 4 was more rapid, followed by slower long-term rates (the corresponding modeled pH evolution is provided in Fig. S4). To fit the data requires an increase in v_{Mg} by a factor of 3 and a decrease in $R_{>SiO_2}$ by a factor of 4.5. Although we cannot determine uniquely whether the decrease was associated with the attachment or detachment rate of $>SiO_2$, to account for the lower Si concentrations requires an increase in $k_{>SiO_2}$ by a factor of 50. This is because increasing $k_{>SiO_2}$ more strongly impacts the steady-state Mg release rate, while decreasing $v_{>SiO_2}$ impacts both early and steady-state Mg and Si rates (*cf.* Fig. S3). The Mg isotopes also place constraints on v_{Mg} as discussed in Section 4.4. However, the rapid increase in Mg concentrations appears to require an increase in the thickness of the active layer (AL) relative to the experiments that contained a supporting electrolyte (Fig. 5C and D). These changes in rate coefficients result in a decrease in the overall olivine dissolution rate from $10^{-13.1}$ to $10^{-13.75}$ mol/cm^2/s between the reference model and the corresponding model for experiments 3 and 4 (Table 4). The rate constant for SiO_2(am) precipitation of 3.3×10^{-9} mol/m^2/s, using the olivine surface area, is also in agreement with previously published values at neutral pH (3.1×10^{-9} mol/m^2/s at 60 °C; Rimstidt and Barnes, 1980).

Olivine dissolution rates at steady state have been previously shown to decrease with decreasing ionic strength (I) of the solution. For example Pokrovsky and Schott (2000b) observed a two-fold reduction in rate as I was decreased from 10^{-1} to 10^{-3} M. The surface charge of fresh unreacted Fo91 at low pH also decreases with decreasing I (Pokrovsky and Schott, 2000a), which may allow for more rapid exchange of Mg during early stages of dissolution. Wang and Giammar (2013) also observed that olivine dissolution rates decrease with decreasing NaCl and proposed that a steric effect associated with Na at or near the surface allows protons greater access to the Si-rich layer and promotes the release of Mg^{2+}. The more rapid initial dissolution rates (at <2 days) and slower steady-state dissolution rates (at >2 days) observed here in the absence of an electrolyte are consistent with the above findings. The more rapid initial Mg exchange rate also generates more depletion of Mg in the active layer leading to model Mg/Si of 0.05 in experiments 3 and 4, compared to 0.5 in experiments 1 and 2. Thus, the lower $R_{>SiO_2}$ and increase in $>SiO_2$ concentration in the active layer associated with more rapid Mg exchange create a feedback that reduces the long-term net dissolution rate substantially, despite the lower pH in these experiments (see also Fig. S3). To determine the precise nature of the dependence of v_{Mg} and $v_{>SiO_2}$ on supporting electrolyte concentration would require a broader range of experimental conditions and more detailed characterization of surface properties over time.

Experiments 2R, 19S, and 19R, conducted with larger olivine grains, show similar behavior and are well described by the model after adjustment of some rate parameters (Fig. 6). For experiments 2R and 19R, the data are best fit with a v_{Mg} that is a factor of 3 greater than in the reference model but within the uncertainty, while $R_{>SiO_2}$ and the associated Si rate parameters remained consistent with the reference model. Overall rates are comparable to those determined for experiments 1 and 2. In contrast, for the un-mixed experiment 19-S, both v_{Mg} and $R_{>SiO_2}$ are slower by a factor of 6 and 10, respectively, compared to the well-mixed experiments. The experiments also yield net dissolution rates that are nearly an order of magnitude slower than those determined for the rocking experiments. This difference in rate may reflect chemical gradients that decrease both transport of H^+ to the surface and transport of SiO_2 away from the surface, and are not captured using the bulk solution properties. Under these conditions, the calculated rates are effective rates that include transport effects. The data and modeling approach presented here do not allow us to constrain the full dynamics of transport effects (*e.g.*, Li et al., 2008; DePaolo, 2011).

4.3.1. Overall dissolution rates and comparison to previous studies

The model rate profiles for net Mg and Si release (*i.e.* $R_{>SiO_2} - R_{SiO_2}$) are shown as a function of time, pH, and

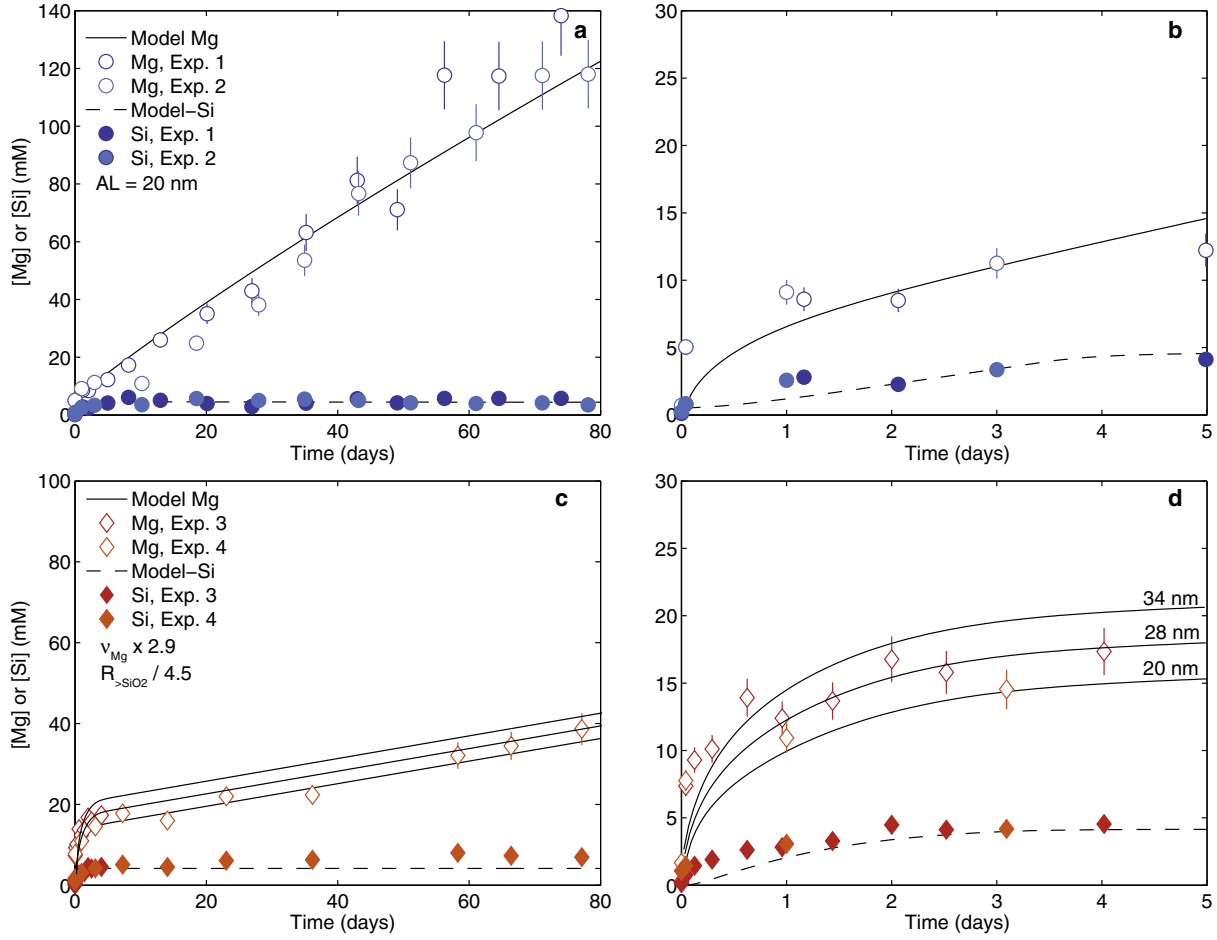

Fig. 5. Model fit to experiments 1–4. Magnesium (open symbols) and Si (closed symbols) over the full experimental duration are shown in (A), and during the initial incongruent dissolution phase in (B). The model fit to the combination of experiments 1 and 2 in (A) is considered the reference model. The same scheme is applied in (C) and (D) where model results for experiments 3 and 4 are presented. The changes in rate coefficients are indicated and the thickness of the active layer (*AL*, nm) is indicated. For experiments 3 and 4, a sensitivity analysis showing variation in the *AL* is provided. All experiments were conducted at 100 bar CO_2 and 60 °C in the presence of 0.5 M NaCl (Johnson et al., 2014).

SiO_2(aq) in Fig. 7 for experiments 1 and 2. Early in the experiments, Mg release rates are substantially greater than Si. In the model, this occurs because the rate of Si dissolution depends on the formation of $>SiO_2$ sites via the Mg exchange reaction (Eqs. (7) and (11)). Conceptually, the greater release rate of Mg compared to Si is attributed to the weaker Mg–O bonds relative to Si–O bonds. The atomic-level explanation for this preferential bond breakage might involve an associative mechanism in which one or more protons bond to an oxygen in the olivine near-surface region, which is nominally bonded to three Mg^{2+} ions in octahedral coordination and one Si^{4+} in tetrahedral coordination in the olivine crystal structure. The resulting inductive effect, in which the more electronegative proton (2.2 on the Pauling scale) relative to Mg (Pauling electronegativity of 1.3) pulls electron density out of the Mg–O bonds, results in their lengthening and breakage due to temporary overbonding of the oxygen. The loss of each Mg^{2+} from the olivine structure would require its replacement by two protons, resulting in a major disruption of the olivine structure due to inductive (electron withdrawing) and electrostatic (repulsive) effects. Thus, formation of H–O bonds in olivine would lead to lengthening and eventual breakage of the Si–O bond. Although no Si–O bond breakage is required if SiO_4 tetrahedra were released to aqueous solution, polymerization of SiO_4 tetrahedra to form a Mg-depleted, Si-enriched amorphous layer would require Si–O bond breakage. At lower pH, the incorporation of protons into octahedral sites to replace Mg should be enhanced, thus resulting in higher Mg release rates. This is accounted for in the model through the dependence of Reaction (1) on H^+. However, this atomistic model does not easily explain why steady-state stoichiometric dissolution is achieved in the experiments and in the surface kinetic model. Such an explanation would require a more complex mechanism, likely involving the effects of up to six protons replacing the three Mg^{2+} ions bonded to each oxygen in olivine, which could lead to such rapid breakage of the Si–O bond that stoichiometric dissolution is ultimately achieved. The simplified macroscopic surface kinetic model formula-

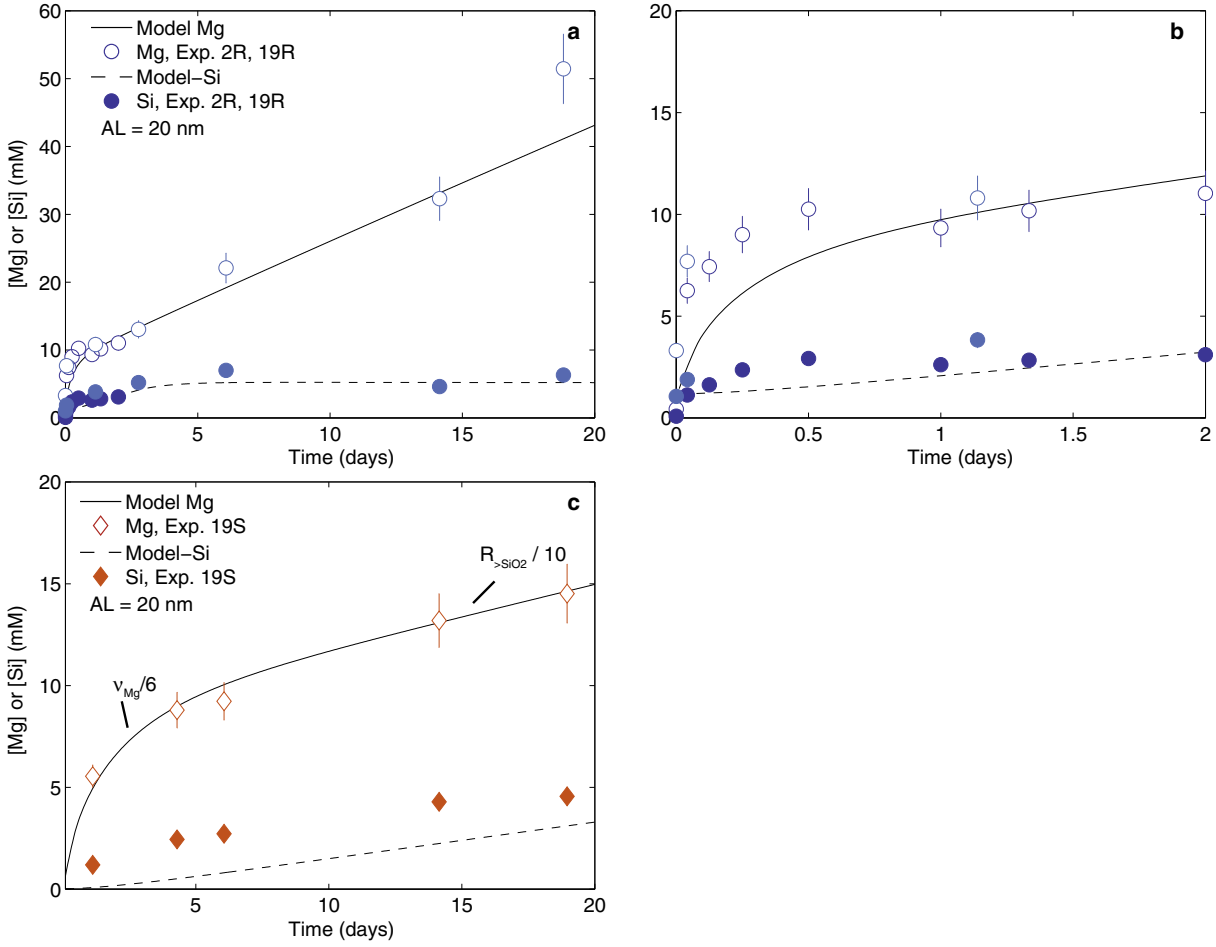

Fig. 6. Model fit to the combined experiments 2R and 19R (well mixed) are shown over the full experimental duration (A), and during the initial incongruent dissolution phase in (B). Model fit to experiments 19S (unmixed) (C). The changes in rate coefficients relative to the reference model are indicated. All experiments were conducted at 100 bar and 60 °C in the presence of 0.5 M NaCl.

tion presented here suggests that as Mg is preferentially removed from the active layer, $R_{>SiO_2}$ is initially very low due to low $>SiO_2$ abundance in the active layer and increases as Mg exchange proceeds. As further Mg is removed, the Mg/Si in the active layer decreases, reducing R_{Mg}. The attainment of stoichiometric steady-state dissolution in Fig. 7 thus results from the stabilizing feedback among the Mg/Si of the active layer, aqueous Si concentrations, and the ion-specific rates (*i.e.* Eqs. (5)–(7) and (9)–(11)). In other words, the steady state stoichiometric dissolution emerges naturally from the kinetic description of the atomistic processes.

For olivine, the breaking of Si–O bonds at low pH is typically designated as the rate limiting reaction for the reasons discussed above. However, our modeling results suggest that the overall dependence of the dissolution rate on Mg and Si dynamics is complex (Fig. 8A, Fig. S3). When we couple the individual steps in the dissolution (Reactions (1) and (2)) through the composition of the surface layer (Eqs. (9) through (11)), the processes that control the overall rate become more complex and it is not straight-forward to assign a single rate constant or rate-limiting reaction. In other words, the coupling imposed by Reactions (1)–(3) exerts a strong control on the overall rate. This is shown conceptually by individually varying the individual rate constants and running the model to steady-state rates (Fig. 8A). An additional sensitivity analysis is presented in Fig. S3. As v_{Mg} increases, the overall dissolution rate increases. This is because the removal of Mg increases $P_{>SiO_2}$ and by extension $R_{>SiO_2}$ (Eqs. (7) and (11)). Similarly, there is a stronger positive relationship between $v_{>SiO_2}$ and the overall dissolution rate, and the inverse is true for $k_{>SiO_2}$. The initiation of a plateau in the overall rate at high $v_{>SiO_2}$ is presumably because Mg exchange eventually becomes limiting. Such conditions may occur at high pH (Pokrovsky and Schott, 2000b). Finally the dependence of the overall rate on k_{SiO_2} is weaker, but occurs because net SiO_2(am) precipitation impacts $R_{>SiO_2}$ by controlling the attachment rate of $>SiO_2$ once SiO_2(am) saturation is reached.

Although we only assign a pH dependence to the Mg exchange reaction, because of the couplings described above the predicted steady-state model produces a pH dependence in overall rates consistent with the observed

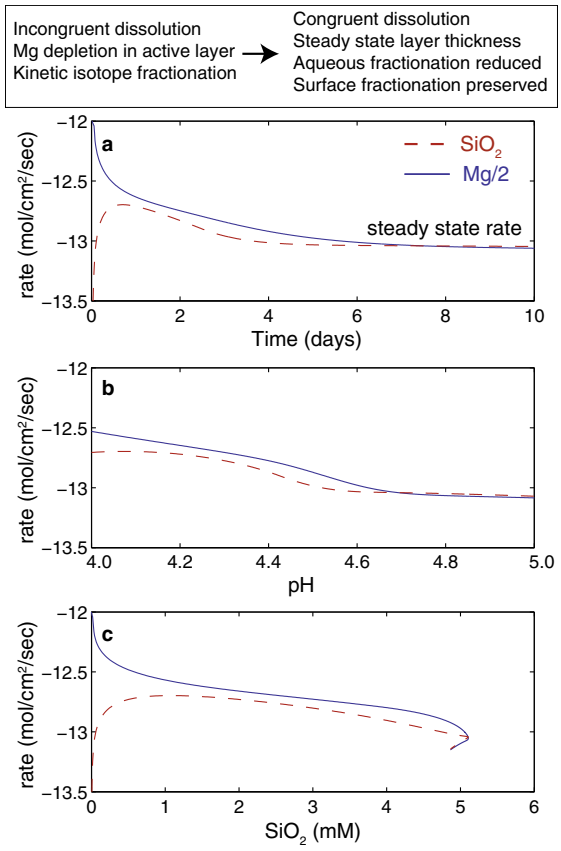

Fig. 7. Rate profiles as a function of (A) time; (B) pH; and (C) $SiO_{2(aq)}$ concentrations for the reference model. The bar at top indicates the dominant processes occurring from initial to steady-state dissolution.

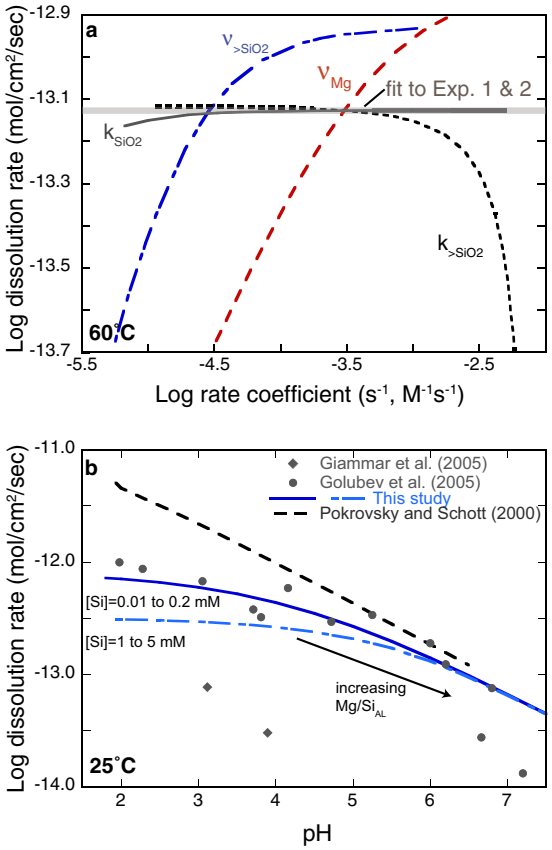

Fig. 8. (A) Sensitivity of the steady-state dissolution rate to the individual rate coefficients. Each rate coefficient was varied independently while the others were held constant at the values determined for the reference model (see Table 4). The best fit to experiments 1 and 2 is shown by the gray horizontal bar. (B) Comparison of general model behavior to data for low-temperature olivine dissolution in the presence of CO_2 under flow-through conditions (Golubev et al., 2005) and the model of Pokrovsky and Schott (2000b), calculated assuming $[H^+]^{0.37}$ in order to facilitate comparison between model formulations. For the surface kinetic model with the Mg exchange rate also assumed proportional to $[H^+]^{0.37}$, the resulting dependence of the overall dissolution rate on H^+ concentration at Si concentration <0.01 mM is ~0.21. The ratios of the individual rate constants determined at 60 °C were held constant from the reference model but decreased to fit the lower temperature data; however, the rate constants likely have slightly different temperature dependences.

pH dependence of dissolution rates in the presence of CO_2 (Fig. 8B). As above, the Mg release rate in the model influences the detachment rate of Si by moderating the concentration of $>SiO_2$. As the Si concentration in solution increases (*e.g.*, lower flow rates) the dissolution rates at low pH plateau, resulting in a weaker dependence on pH as the rate of net Si release becomes more important. This appears to be consistent with results for closed-system reactors (Wang and Giammar, 2013; Johnson et al., 2014). Finally, as the pH increases, the Mg/Si in the active layer also increases because of slower Mg release rates, in turn decreasing $R_{>SiO_2}$.

4.3.2. Consequences of spatial discretization and implications for rate coefficients

Determination of all kinetic parameters is subject to assumptions made regarding the reactive surface area, and other factors that contribute to the observed overall ion release rate (*e.g.*, the dependence of overall rate on pH, reaction affinity and ionic strength). Here, the observed Mg release rate was reproduced according to the values assigned to represent the V_{AL}, ν_{Mg}, and P_{Mg} (which is partly a function of $R_{>SiO_2}$). As noted previously, the HR-TEM profiles show remarkable nanometer-scale complexity. In contrast, the boundary conditions in the model assume that stoichiometric olivine was supplied to the active layer as $>SiO_2$ was removed from the surface. Because the balance between solid-state diffusion and interfacial dissolution and re-precipitation cannot be resolved from our HR-TEM data, this assumption was necessary. Below we qualitatively describe the uncertainty arising from this assumption. In addition, we find that the rate coefficients differ in the presence or absence of a supporting electrolyte. As a consequence, the rate parameters provided in Table 4 should be considered "effective" rate coefficients applicable to the specific experimental conditions.

Although the model reproduces the solution composition convincingly, we further evaluate the solid phase mass

balance because the solid phase stoichiometry is coupled to the rate coefficients via Eqs. (9)–(11). In order to calculate the maximum amount of Mg removal from the HR-TEM profiles, we assume constant volume replacement and that Si is conservative throughout the altered layers (*cf.* Fig. 4C). The resulting difference between the HR-TEM and the model active layer is 29% and 12% for 19R and 19S respectively, which is reasonable given that the HR-TEM results represent a maximum estimate of Mg depletion. The consequence of preserving the mass balance through averaging the active layer concentration is that the value of P_{Mg} is artificially low (and $P_{>SiO_2}$ is high) and measured concentration gradients are averaged. These underlying assumptions are embedded in the effective rate coefficients. However, effective rate coefficients can still be useful if they capture the key processes: the model successfully reproduces both initial incongruent dissolution and steady-state dissolution, as well as the formation of altered surface layers. For olivine, given that most of the Mg depletion occurs within the active layer, where Mg/Si ratios drop from ca. 1.5 to 0.2 over approximately 30 nm, our treatment of only the active layer appears reasonable. However, more studies that provide HR-TEM constraints on composition and crystallinity of the surface as a function of depth, combined with spatially resolved models that account for solid-state interdiffusion (*e.g.*, Yang et al., 2009), may yield further insights into the importance of the amorphous-crystalline transitions zone for the evolution of the active layer, overall dissolution kinetics and isotopic fractionation.

4.4. Isotopic fractionation and surface layer evolution during dissolution

The rapid increase in dissolved Mg relative to Si observed in the early stages of the experiment is correctly reproduced in the model through the creation of a Si-rich and Mg-depleted active layer as indicated by HR-TEM analyses (Daval et al., 2011). Fig. 9A shows the predicted change in Mg/Si of the active layer (Mg/Si_{AL}) from stoichiometric values of 1.84 to steady-state values of approximately 0.05 in experiment 3. For comparison, in experiments 1 and 2, with more rapid net dissolution rates but lower Mg exchange rates, the Mg/Si_{AL} is much higher and stabilizes at values closer to 0.3. The δ^{26}Mg in experiment 3 also showed increasing values over time that finally approach the value of the starting olivine. Thus, we assume that the initial ^{24}Mg enrichment in solution reflects a preferential breaking of ^{24}Mg–O bonds resulting in a kinetic isotope effect.

The δ^{26}Mg of the active layer ($\delta^{26}Mg_{AL}$) and dissolved Mg evolve in unison. Values of $\alpha_{Mg\text{-}Fo}$ of between 0.9995 and 0.999 are consistent with the observed isotopic variation in the dissolved Mg (Fig. 9B). In comparison to the dissolved Mg profiles, the model δ^{26}Mg of the surface layer is complex. During the initial stages of reaction, Mg release is most rapid as indicated by the rapid decrease in Mg/Si and corresponding increase in dissolved Mg concentration. Subtle variation in $\delta^{26}Mg_{AL}$ is evident at ~4 days when the Mg/Si depletion reaches steady state. Due to the initially high Mg exchange rate, a maximum in $R_{>SiO_2}$ also occurs coincident with the δ^{26}Mg maximum because $P_{>SiO_2}$ increases more quickly than aqueous SiO_2 concentrations, where the later controls the attachment rate (see Fig. S5 for sensitivity analysis). This results in the early enrichment of ^{26}Mg of the active layer. As the rate of Mg release decreases, an increased supply of Mg to the active layer from the bulk crystal reduces the $\delta^{26}Mg_{AL}$ until eventually a steady-state balance develops between the net release of $>SiO_2$ and the supply of Mg. The slight drop in the $\delta^{26}Mg_{AL}$ after 4 days is thus associated with the attainment of a lower steady-state $R_{>SiO_2}$. Once steady-state dissolution is reached, the dissolved Mg supplied to solution has the isotopic composition of the crystalline olivine due to the presence of the ^{26}Mg-enriched surface and the assigned fractionation factor, hence the measurable fractionation is

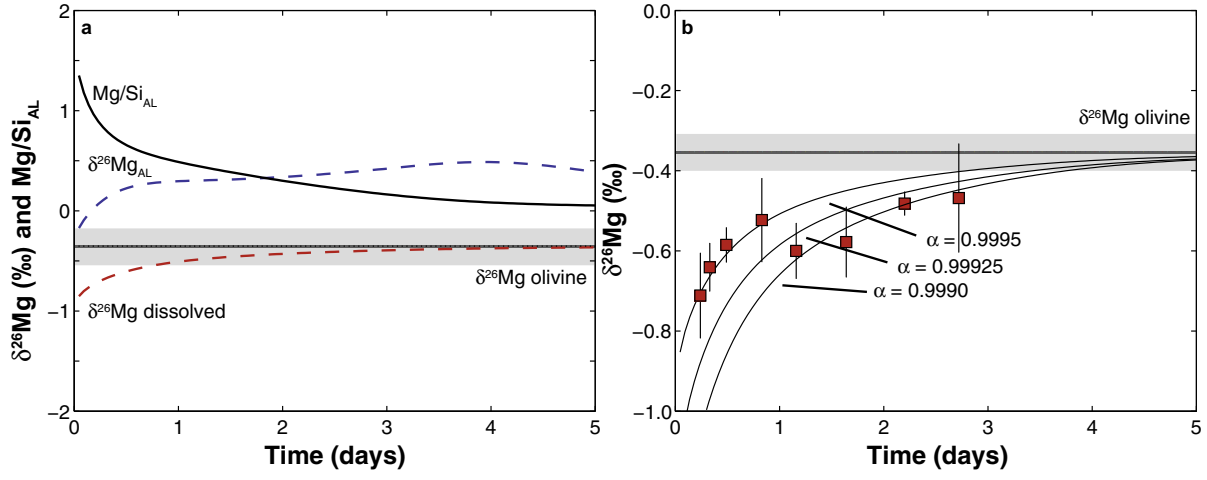

Fig. 9. Model magnesium isotopic and surface layer Mg/Si evolution for experiment 3. (A) The model change in the Mg/Si of the active layer (Mg/Si_{AL}) is shown in comparison to the δ^{26}Mg of the active layer (*AL*) and the dissolved Mg. (B) Comparison between model and measured δ^{26}Mg of the aqueous Mg (uncertainties are represented as 1 s.d.). The best fit to the data is between $\alpha_{Mg\text{-}Fo} = 0.9995$ and 0.9990 and variations in $\alpha_{Mg\text{-}Fo}$ are shown for reference.

no longer preserved in the fluid once a steady state is reached. In contrast, because of the preferential removal of ^{24}Mg, the surface remains permanently enriched in ^{26}Mg by a factor that depends on both v_{Mg} and $\alpha_{Mg\text{-}Fo}$, even though the active layer is penetrating inward over time (Fig. S5).

Although the limited data in this study preclude full evaluation of the Mg isotope systematics, the model suggests that the isotopic composition of dissolved Mg under closed-system conditions is much more sensitive to variations in v_{Mg} compared to variations in V_{AL}, whereas the dissolved Mg responds identically to both (e.g., Fig. S3B,J). In addition, because the early release rate of Mg determines the isotopic fractionation, the isotopes are not appreciably sensitive to the value of $v_{>SiO_2}$. The sensitivity of the isotopes to only one model parameter suggests that isotopic fractionation could provide a useful tool for constraining individual ion exchange rates, even in the absence of HR-TEM constraints. We also assume that secondary processes such as sorption (Opfergelt et al., 2014) have a negligible influence on the dissolved isotopic composition. As the concentration of dissolved Mg is substantial relative to the initial exchangeable Mg, and no other secondary phases were observed in the experimental products (Johnson et al., 2014), this assumption appears reasonable.

The experiments were also conducted only under closed-system conditions where concentrations evolve with time. To explore the ability of the model to reproduce observed Mg, Si and $\delta^{26}Mg$ evolution under flow-through conditions, we applied the model to the data of Wimpenny et al. (2010) using their experimental conditions and reported parameters. In the absence of HR-TEM constraints, we assume an active layer thickness of 20–40 nm (an active layer thickness greater than 12 nm is required to reproduce the observed features). The model suggests a transient period of dissolution in the early stages (<0.5 days) followed by attainment of steady-state release (Fig. 10). The model is also consistent with the observed $\delta^{26}Mg$, although given the limited information and number of measurements, the long-term behavior (*i.e.* attainment of bulk olivine $\delta^{26}Mg$ values) and the value of $\alpha_{Mg\text{-}Fo}$ cannot be precisely constrained. Relative to the closed-system experiments, the flow-through experiments are highly sensitive to the Mg exchange rate and much less sensitive to the Si attachment and detachment kinetics, as suggested in the earlier rate profile analysis (Fig. 10A and C).

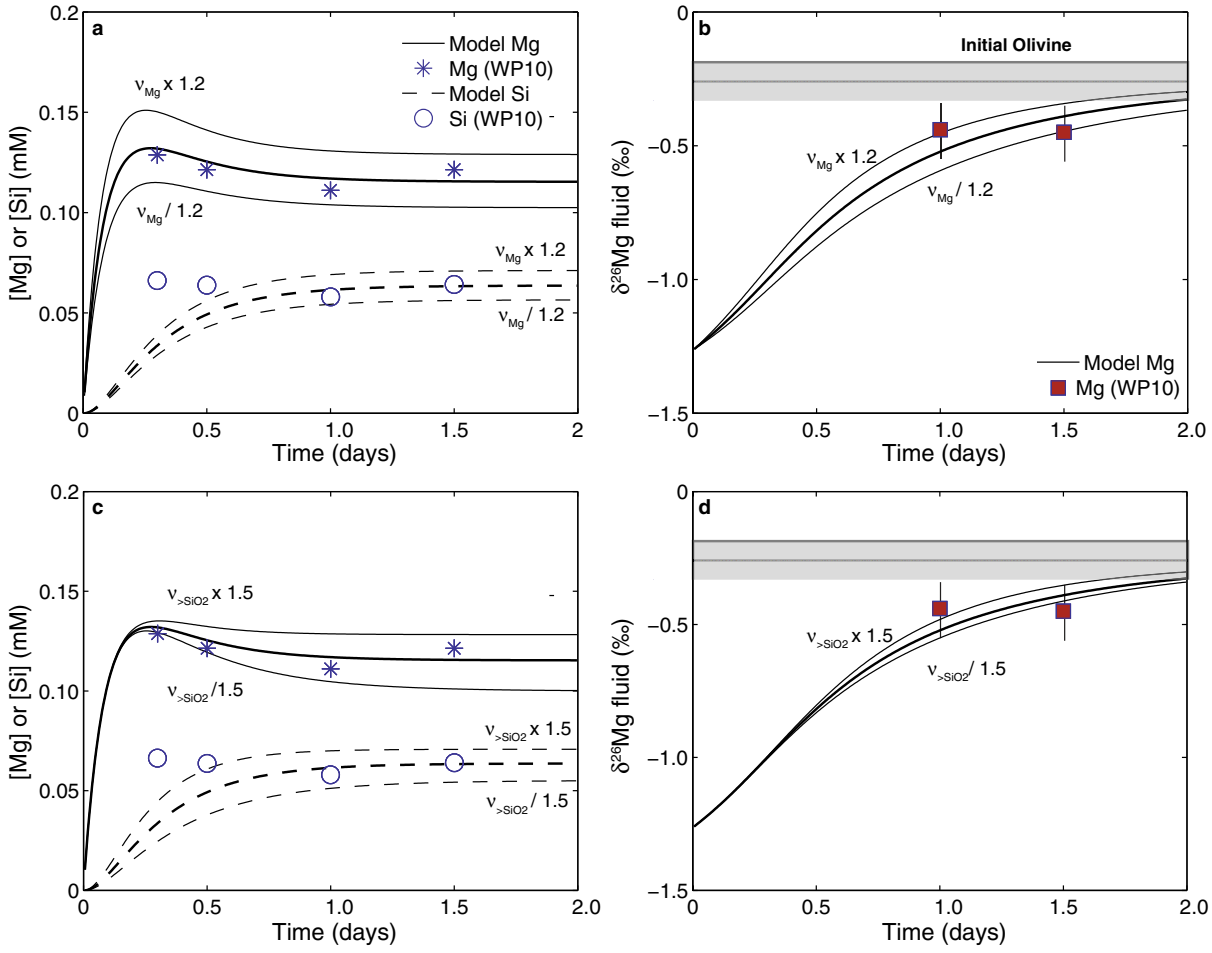

Fig. 10. Model evaluation of Wimpenny et al. (2010) experimental series FO_2 at pH 3 and 25 °C. (A) Model fit for Mg and Si concentrations given variations in v_{Mg} (see parameters in Table 4). (B) Comparison between measured $\delta^{26}Mg$ to model prediction using $\alpha_{Mg\text{-}Fo} = 0.999$. Model fit for Mg and Si concentrations (C) and measured $\delta^{26}Mg$ (D) showing effect of variations in $v_{>SiO_2}$.

4.5. Implications for natural systems

It is likely that the kinetic isotope fractionation observed and modeled here occurs during the dissolution of many minerals, although it may not be observable under all conditions. However, if several layers are active then an isotopically depleted layer may be maintained indefinitely on mineral surfaces. The slower the preferential release rate of the element is relative to the migration of the active layer, the more strongly the fractionation will be expressed within the mineral surface. In other words, the composition of the surface layer is a function of both the kinetic fractionation factor and the rate of release of the element. In most natural systems, isotopic fractionation is likely not observable in fluids as it occurs over a short time interval associated with transient dissolution and evolution of the surface layer. Similarly, the enrichment of the surface layer may not be detectable in bulk analyses, although selective leaching procedures may access isotopically altered surfaces.

The importance of the composition of the surface layer extends beyond the isotopes: the model predicts that net rates of Mg and Si release are coupled through the composition of the surface layer. This enables the model to account for the pH dependence of overall dissolution rates and the effect of increasing concentrations of aqueous Si. Although the model is applied to here to specific experiments, we show how it can be used to predict steady-state olivine dissolution rates across a broad range of pH values if appropriate rate constants and active layer thicknesses are determined (Fig. 8B). Flow through low-permeability ultramafic and mafic rocks will result in compositional gradients in the fluid such that accounting for the role of pH and aqueous Si may be important for predicting rates in natural systems.

5. CONCLUSIONS

Descriptive models of silicate mineral dissolution must be balanced against their utility for describing complex multi-component open systems. Kinetic models for silicate mineral dissolution have been largely based on a simplified version of Transition State Theory (TST), where the overall dissolution rate is equal to the product of the kinetic rate constant, surface area, the reaction affinity, and the activity of ions that inhibit or accelerate dissolution. However, for complex silicate minerals such as olivine and many other major rock-forming minerals, the coupling among different reactions to determine the composition of the dissolving layer may be as important as reaction affinity in determining the overall dissolution rate.

The model approach used here also suggests that no single reaction is rate limiting, but rather the relationships between various components, over space and time, determine the overall forsterite dissolution rate. For example, the dissolution of repolymerized SiO_4 tetrahedra regulates the supply of Mg to the active layer, while the net exchange of Mg for protons controls the rate of re-polymerization of SiO_4 tetrahedra, leading to net mineral dissolution. The interdependency of these processes appears to explain the order of magnitude variation in overall dissolution rates we observed and modeled. The possibility that similar processes may occur in other silicate minerals is supported by the observation of kinetic isotope effects during the dissolution of amphiboles and micas; however in such cases the inter-relationship among individual components may be more complex.

The approach presented here represents a model of moderate complexity that affords an evaluation of the coupling between the fluxes of individual ions and the overall dissolution rate of olivine. Such an approach may be advantageous in extracting rates from experimental data and as an interpretive tool for probing the interconnection among key reactions. Although parameterizing the rate equations does require more information, the approach presented here could still provide an alternative rate law for geochemical and reactive transport models applicable at the continuum scale (*e.g.*, Druhan et al., 2013). Ideally, such approaches might lead to improved models of mineral–fluid interactions across a range of geological environments.

ACKNOWLEDGMENTS

We acknowledge the Global Climate and Energy Project (GCEP-48942) at Stanford University for funding the work presented here. We acknowledge J. Schott, J. Wimpenny, D. Daval, several anonymous reviewers, and the Earth Surface Geochemistry group at GFZ Potsdam for comments and discussions that greatly improved the manuscript. We also acknowledge the technical support of the staff of the Stanford ICPMS, Environmental Measurements-1 and the Stanford Nanocharacterization Laboratories.

APPENDIX A. SUPPLEMENTARY DATA

Supplementary data associated with this article can be found, in the online version, at http://dx.doi.org/10.1016/j.gca.2015.11.019.

REFERENCES

Baker J., Bizzarro M., Wittig N., Connelly J. and Haack H. (2005) Early planetesimal melting from an age of 4.5662 Gyr for differentiated meteorites. *Nature* **436**, 1127–1131.

Bearat H., McKelvy M. J., Chizmeshya A. V. G., Gormley D., Nunez R., Carpenter R. W., Squires K. and Wolf G. H. (2006) Carbon sequestration via aqueous olivine mineral carbonation: role of passivating layer formation. *Environ. Sci. Technol.* **40**, 4802–4808.

Bourg I. C., Richter F. M., Christensen J. N. and Sposito G. (2010) Isotopic mass dependence of metal cation diffusion coefficients in liquid water. *Geochim. Cosmochim. Acta* **74**, 2249–2256.

Brantley S. L., Liermann L. and Bullen T. D. (2001) Fractionation of Fe isotopes by soil microbes and organic acids. *Geology* **29**, 535–538.

Brantley S. L., Liermann L. J., Guynn R. L., Anbar A., Icopini G. A. and Barling J. (2004) Fe isotopic fractionation during mineral dissolution with and without bacteria. *Geochim. Cosmochim. Acta* **68**, 3189–3204.

Casey W. H. and Bunker B. (1990) Leaching of mineral and glass surfaces during dissolution, vol. 23. In *Mineral-Water Interface*

Geochemistry, Rev. Mineral (eds. M. F. Hochella, Jr. and A. F. White). pp. 397–426.

Casey W. H., Westrich H. R. and Arnold G. W. (1988) Surface-chemistry of labradorite feldspar reacted with aqueous-solutions at pH = 2, 3, and 12. *Geochim. Cosmochim. Acta* **52**, 2795–2807.

Chou L. and Wollast R. (1984) Study of the weathering of albite at room-temperature and pressure with a fluidized-bed reactor. *Geochim. Cosmochim. Acta* **48**, 2205–2217.

Daval D., Sissmann O., Menguy N., Saldi G. D., Guyot F., Martinez I., Corvisier J., Garcia B., Machouk I., Knauss K. G. and Hellmann R. (2011) Influence of amorphous silica layer formation on the dissolution rate of olivine at 90 °C and elevated pCO_2. *Chem. Geol.* **284**, 193–209.

Daval D., Hellmann R., Martinez I., Gangloff S. and Guyot F. (2013) Lizardite serpentine dissolution kinetics as a function of pH and temperature, including effects of elevated pCO_2. *Chem. Geol.* **351**, 245–256.

DePaolo D. J. (2011) Surface kinetic model for isotopic and trace element fractionation during precipitation of calcite from aqueous solutions. *Geochim. Cosmochim. Acta* **75**, 1039–1056.

Druhan J. L., Steefel C. I., Williams K. H. and DePaolo D. J. (2013) Calcium isotope fractionation in groundwater: molecular scale processes influencing field scale behavior. *Geochim. Cosmochim. Acta* **119**, 93–116.

Duan Z. H. and Sun R. (2003) An improved model calculating CO_2 solubility in pure water and aqueous NaCl solutions from 273 to 533 K and from 0 to 2000 bar. *Chem. Geol.* **193**, 257–271.

Galy A., Yoffe O., Janney P. E., Williams R. W., Cloquet C., Alard O., Halicz L., Wadhwa M., Hutcheon I. D., Ramon E. and Carignan J. (2003) Magnesium isotope heterogeneity of the isotopic standard SRM980 and new reference materials for magnesium-isotope-ratio measurements. *J. Anal. At. Spectrom.* **18**, 1352–1356.

Giammar D. E., Bruant R. G. and Peters C. A. (2005) Forsterite dissolution and magnesite precipitation at conditions relevant for deep saline aquifer storage and sequestration of carbon dioxide. *Chem. Geol.* **217**, 257–276.

Golubev S. V., Pokrovsky O. S. and Schott J. (2005) Experimental determination of the effect of dissolved CO_2 on the dissolution kinetics of Mg and Ca silicates at 25 °C. *Chem. Geol.* **217**, 227–238.

Handler M. R., Baker J. A., Schiller M., Bennett V. C. and Yaxley G. M. (2009) Magnesium stable isotope composition of Earth's upper mantle. *Earth Planet. Sci. Lett.* **282**, 306–313.

Hartmann J., West A. J., Renforth P., Koehler P., De La Rocha C. L., Wolf-Gladrow D. A., Duerr H. H. and Scheffran J. (2013) Enhanced chemical weathering as a geoengineering strategy to reduce atmospheric carbon dioxide, supply nutrients, and mitigate ocean acidification. *Rev. Geophys.* **51**, 113–149.

Hellmann R. (1997) The albite-water system. 4. Diffusion modeling of leached and hydrogen-enriched layers. *Geochim. Cosmochim. Acta* **61**, 1595–1611.

Hellmann R., Wirth R., Daval D., Barnes J. P., Penisson J. M., Tisserand D., Epicier T., Florin B. and Hervig R. L. (2012) Unifying natural and laboratory chemical weathering with interfacial dissolution and reprecipitation: a study based on the nanometer-scale chemistry of fluid-silicate interfaces. *Chem. Geol.* **294–295**, 203–216.

Huang F., Glessner J., Ianno A., Lundstrom C. and Zhang Z. (2009) Magnesium isotopic composition of igneous rock standards measured by MC-ICP-MS. *Chem. Geol.* **268**, 15–23.

Jambor J. L., Dutrizac J. E. and Raudsepp M. (2007) Measured and computed neutralization potentials from static tests of diverse rock types. *Environ. Geol.* **52**, 1019–1031.

Jarvis K., Carpenter R. W., Windman T., Kim Y., Nunez R. and Alawneh F. (2009) Reaction mechanisms for enhancing mineral sequestration of CO_2. *Environ. Sci. Technol.* **43**, 6314–6319.

Johnson J. W., Oelkers E. H. and Helgeson H. C. (1992) SUPCRT92: a software package for calculating the standard molal thermodynamic properties of minerals, gases, aqueous species, and reactions from 1 to 5000 bar and 0 to 1000 °C. *Comput. Geosci.* **18**, 899–947.

Johnson N. C., Thomas B., Maher K., Rosenbauer R. J., Bird D. K. and Brown, Jr., G. E. (2014) Olivine dissolution and carbonation rates at 60 °C and 100 bar. *Chem. Geol.* **373**, 93–105.

Kiczka M., Wiederhold J. G., Frommer J., Kraemer S. M., Bourdon B. and Kretzschmar R. (2010) Iron isotope fractionation during proton- and ligand-promoted dissolution of primary phyllosilicates. *Geochim. Cosmochim. Acta* **74**, 3112–3128.

King H. E., Plumper O. and Putnis A. (2010) Effect of secondary phase formation on the carbonation of olivine. *Environ. Sci. Technol.* **44**, 6503–6509.

King H. E., Satoh H., Tsukamoto K. and Putnis A. (2014) Surface-specific measurements of olivine dissolution by phase-shift interferometry. *Am. Mineral.* **99**, 377–386.

Koehler P., Hartmann J. and Wolf-Gladrow D. A. (2010) Geoengineering potential of artificially enhanced silicate weathering of olivine. *Proc. Natl. Acad. Sci. U.S.A.* **107**, 20228–20233.

Lasaga A. C. and Luttge A. (2004) Mineralogical approaches to fundamental crystal dissolution kinetics. *Am. Mineral.* **89**, 527–540.

Li D. and Duan Z. (2007) The speciation equilibrium coupling with phase equilibrium in the H_2O–CO_2–NaCl system from 0 to 250 °C, from 0 to 1000 bar, and from 0 to 5 molality of NaCl. *Chem. Geol.* **244**, 730–751.

Li L., Steefel C. I. and Yang L. (2008) Scale dependence of mineral dissolution rates within single pores and fractures. *Geochim. Cosmochim. Acta* **72**, 360–377.

Loring J. S., Thompson C. J., Wang Z., Joly A. G., Sklarew D. S., Schaef H. T., Ilton E. S., Rosso K. M. and Felmy A. R. (2011) In situ infrared spectroscopic study of forsterite carbonation in wet supercritical CO_2. *Environ. Sci. Technol.* **45**, 6204–6210.

Luce R. W., Bartlett R. W. and Parks G. A. (1972) Dissolution kinetics of magnesium silicates. *Geochim. Cosmochim. Acta* **36**, 35–50.

Nielsen L. C., DePaolo D. J. and De Yoreo J. J. (2012) Self-consistent ion-by-ion growth model for kinetic isotopic fractionation during calcite precipitation. *Geochim. Cosmochim. Acta* **86**, 166–181.

Nielsen L. C., De Yoreo J. J. and DePaolo D. J. (2013) General model for calcite growth kinetics in the presence of impurity ions. *Geochim. Cosmochim. Acta* **115**, 100–114.

Oelkers E. H. (2001) An experimental study of forsterite dissolution rates as a function of temperature and aqueous Mg and Si concentrations. *Chem. Geol.* **175**, 485–494.

Oelkers E. H. and Cole D. R. (2008) Carbon dioxide sequestration: a solution to a global problem. *Elements* **4**, 305–310.

Olsson J., Bovet N., Makovicky E., Bechgaard K., Balogh Z. and Stipp S. L. S. (2012) Olivine reactivity with CO_2 and H_2O on a microscale: implications for carbon sequestration. *Geochim. Cosmochim. Acta* **77**, 86–97.

Opfergelt S., Burton K. W., Georg R. B., West A. J., Guicharnaud R. A., Sigfusson B., Siebert C., Gislason S. R. and Halliday A. N. (2014) Magnesium retention on the soil exchange complex controlling Mg isotope variations in soils, soil solutions and vegetation in volcanic soils, Iceland. *Geochim. Cosmochim. Acta* **125**, 110–130.

Parkhurst D. L. and Appelo C. A. J. (1999) *User's Guide to PHREEQC (Version 2) – A Computer Program for Speciation, Batch-reaction, One-dimentional Transport, and Inverse Geochemical Calculations. U.S. Geological Survey Water-Resources Investigations Report 99-4259*. Denver, Colorado.

Pearce C. R., Saldi G. D., Schott J. and Oelkers E. H. (2012) Isotopic fractionation during congruent dissolution, precipitation and at equilibrium: evidence from Mg isotopes. *Geochim. Cosmochim. Acta* **92**, 170–183.

Petit J. C., Dellamea G., Dran J. C., Magonthier M. C., Mando P. A. and Paccagnella A. (1990) Hydrated-layer formation during dissolution of complex silicate-glasses and minerals. *Geochim. Cosmochim. Acta* **54**, 1941–1955.

Pokrovsky O. S. and Schott J. (2000a) Forsterite surface composition in aqueous solutions: a combined potentiometric, electrokinetic, and spectroscopic approach. *Geochim. Cosmochim. Acta* **64**, 3299–3312.

Pokrovsky O. S. and Schott J. (2000b) Kinetics and mechanism of forsterite dissolution at 25 °C and pH from 1 to 12. *Geochim. Cosmochim. Acta* **64**, 3313–3325.

Putnis A. (2009) Mineral replacement reactions. In *Thermodynamics and Kinetics of Water–Rock Interaction* (eds. E. H. Oelkers and J. Schott). pp. 87–124.

Rasband W. (1997). *U. S. Natl. Institutes Heal.* Bethesda, Maryland, USA. URL http://imagej.nih.gov/ij/.

Richter F. M., Mendybaev R. A., Christensen J. N., Hutcheon I. D., Williams R. W., Sturchio N. C. and Beloso A. D. (2006) Kinetic isotopic fractionation during diffusion of ionic species in water. *Geochim. Cosmochim. Acta* **70**, 277–289.

Rimstidt J. D. and Barnes H. L. (1980) The kinetics of silica-water reactions. *Geochim. Cosmochim. Acta* **44**, 1683–1699.

Rimstidt J. D., Brantley S. L. and Olsen A. A. (2012) Systematic review of forsterite dissolution rate data. *Geochim. Cosmochim. Acta* **99**, 159–178.

Rosenbauer R. J., Bischoff J. L. and Radtke A. S. (1983) Hydrothermal alteration of graywacke and basalt by 4 molal NaCl. *Econ. Geol.* **78**, 1701–1710.

Rosenbauer R. J., Koksalan T. and Palandri J. L. (2005) Experimental investigation of CO_2-brine-rock interactions at elevated temperature and pressure: implications for CO_2 sequestration in deep-saline aquifers. *Fuel Process. Technol.* **86**, 1581–1597.

Ruiz-Agudo E., Putnis C. V., Rodriguez-Navarro C. and Putnis A. (2012) Mechanism of leached layer formation during chemical weathering of silicate minerals. *Geology* **40**, 947–950.

Ruiz-Agudo E., Putnis C. V. and Putnis A. (2014) Coupled dissolution and precipitation at mineral–fluid interfaces. *Chem. Geol.* **383**, 132–146.

Saldi G. D., Daval D., Morvan G. and Knauss K. G. (2013) The role of Fe and redox conditions in olivine carbonation rates: an experimental study of the rate limiting reactions at 90 and 150 °C in open and closed systems. *Geochim. Cosmochim. Acta* **118**, 157–183.

Schott J. and Berner R. A. (1983) X-ray photoelectron studies of the mechanism of iron silicate dissolution during weathering. *Geochim. Cosmochim. Acta* **47**, 2233–2240.

Schott J., Berner R. A. and Sjoberg E. L. (1981) Mechanism of pyroxene and amphibole weathering. 1. Experimental studies of iron-free minerals. *Geochim. Cosmochim. Acta* **45**, 2123–2135.

Schott J., Pokrovsky O. S., Spalla O., Devreux F., Gloter A. and Mielczarski J. A. (2012) Formation, growth and transformation of leached layers during silicate minerals dissolution: the example of wollastonite. *Geochim. Cosmochim. Acta* **98**, 259–281.

Sissmann O., Daval D., Brunet F., Guyot F., Verlaguet A., Pinquier Y., Findling N. and Martinez I. (2013) The deleterious effect of secondary phases on olivine carbonation yield: insight from time-resolved aqueous-fluid sampling and FIB-TEM characterization. *Chem. Geol.* **357**, 186–202.

Sleep N. H., Meibom A., Fridriksson T., Coleman R. G. and Bird D. K. (2004) H_2-rich fluids from serpentinization: geochemical and biotic implications. *Proc. Natl. Acad. Sci. U.S.A.* **101**, 12818–12823.

Stillings L. L. and Brantley S. L. (1995) Feldspar dissolution at 25 °C and pH3: reaction stoichiometry and the effect of cations. *Geochim. Cosmochim. Acta* **59**, 1483–1496.

Teng F.-Z., Wadhwa M. and Helz R. T. (2007) Investigation of magnesium isotope fractionation during basalt differentiation: implications for a chondritic composition of the terrestrial mantle. *Earth Planet. Sci. Lett.* **261**, 84–92.

Verney-Carron A., Vigier N. and Millot R. (2011) Experimental determination of the role of diffusion on Li isotope fractionation during basaltic glass weathering. *Geochim. Cosmochim. Acta* **75**, 3452–3468.

Wang F. and Giammar D. E. (2013) Forsterite dissolution in saline water at elevated temperature and high CO_2 pressure. *Environ. Sci. Technol.* **47**, 168–173.

Watkins J. M., Nielsen L. C., Ryerson F. J. and DePaolo D. J. (2013) The influence of kinetics on the oxygen isotope composition of calcium carbonate. *Earth Planet. Sci. Lett.* **375**, 349–360.

Wiederhold J. G., Kraemer S. M., Teutsch N., Borer P. M., Halliday A. N. and Kretzschmar R. (2006) Iron isotope fractionation during proton-promoted, ligand-controlled, and reductive dissolution of goethite. *Environ. Sci. Technol.* **40**, 3787–3793.

Wimpenny J., Gíslason S. R., James R. H., Gannoun A., Pogge Von Strandmann P. A. E. and Burton K. W. (2010) The behaviour of Li and Mg isotopes during primary phase dissolution and secondary mineral formation in basalt. *Geochim. Cosmochim. Acta* **74**, 5259–5279.

Wogelius R. A. and Walther J. V. (1991) Olivine dissolution at 25 °C – effects of pH, CO_2, and organic-acids. *Geochim. Cosmochim. Acta* **55**, 943–954.

Wolery T. J., Jackson K. J., Bourcier W. L., Bruton C. J., Viani B. E., Knauss K. G. and Delany J. M. (1990) Current status of the EQ3/6 software package for geochemical modeling. *ACS Symp. Ser.* **416**, 104–116.

Wombacher F., Eisenhauer A., Heuser A. and Weyer S. (2009) Separation of Mg, Ca and Fe from geological reference materials for stable isotope ratio analyses by MC-ICP-MS and double-spike TIMS. *J. Anal. At. Spectrom.* **24**, 627.

Yang C. B., Samper J., Zhu C. and Jones S. B. (2009) Numerical modeling of the development of a preferentially leached layer on feldspar surfaces. *Environ. Geol.* **57**, 1639–1647.

Zakaznova-Herzog V. P., Nesbitt H. W., Bancroft G. M. and Tse J. S. (2008) Characterization of leached layers on olivine and pyroxenes using high-resolution XPS and density functional calculations. *Geochim. Cosmochim. Acta* **72**, 69–86.

Ziegler K., Chadwick O. A., Brzezinski M. A. and Kelly E. F. (2005) Natural variations of δ^{30}Si ratios during progressive basalt weathering, Hawaiian Islands. *Geochim. Cosmochim. Acta* **69**, 4597–4610.

Associate editor: Fang-zhen Teng